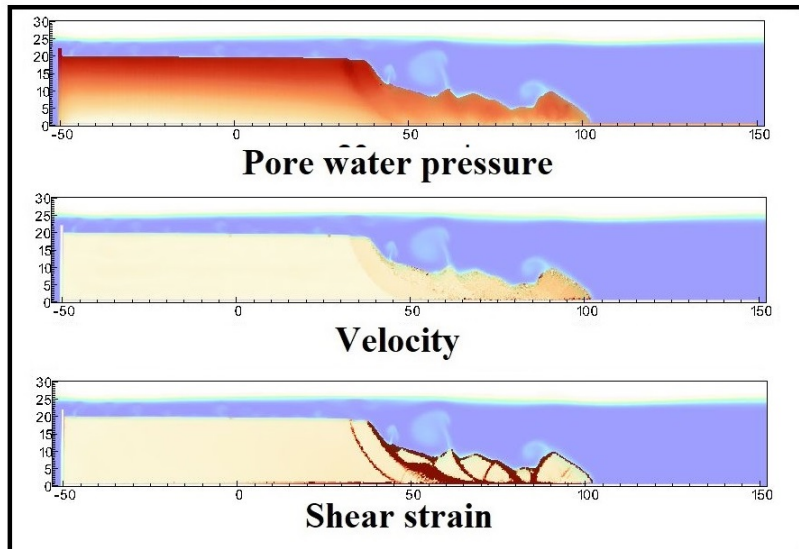


- 1 Graphical Abstract
- 2 MPMICE: A hybrid MPM-CFD model for simulating coupled problems in porous media. Application to earthquake-induced submarine landslides
- 3 Quoc Anh Tran, Gustav Grimstad, Seyed Ali Ghoreishian Amiri



Application to earthquake-induced submarine landslide

₆ Highlights

₇ **MPMICE: A hybrid MPM-CFD model for simulating coupled prob-**
₈ **lems in porous media. Application to earthquake-induced subma-**
₉ **rine landslides**

₁₀ Quoc Anh Tran, Gustav Grimstad, Seyed Ali Ghoreishian Amiri

- ₁₁ • MPMICE is introduced for multiphase flow in porous media.
- ₁₂ • Material Point method allows to model large deformation of non-isothermal
- ₁₃ porous media.
- ₁₄ • ICE (compressible multi-material CFD formulation) allows stabilizing
- ₁₅ pore water pressure and turbulent flow.
- ₁₆ • MPMICE is validated and apply to simulate the earthquake-induced
- ₁₇ submarine landslide.

¹⁸ MPMICE: A hybrid MPM-CFD model for simulating
¹⁹ coupled problems in porous media. Application to
²⁰ earthquake-induced submarine landslides

²¹ Quoc Anh Tran^{a,b}, Gustav Grimstad^a, Seyed Ali Ghoreishian Amiri^a

^a*Norwegian University of Science and Technology, , Trondheim, 7034, Norway*

^b*quoc.a.tran@ntnu.no*

²² **Abstract**

²³ In this paper, we describe a soil-fluid-structure interaction model that com-
²⁴ bines soil mechanics (saturated sediments), fluid mechanics (seawater or air),
²⁵ and solid mechanics (structures). The formulation combines the Material
²⁶ Point Method, which models large deformation of the porous media and the
²⁷ structure, with the Implicit Continuous-fluid Eulerian, which models com-
²⁸ plex fluid flows. We validate the model and simulate the whole process of
²⁹ earthquake-induced submarine landslides. We show that this model captures
³⁰ complex interactions between saturated sediment, seawater, and structure,
³¹ so we can use the model to estimate the impact of potential submarine land-
³² slides on offshore structures.

³³ *Keywords:*

³⁴ Material Point Method, MPMICE, submarine landslide.

35	Contents	
36	Nomenclature	4
37	Introduction	6
38	Theory and formulation	8
39	Assumptions	8
40	Governing equations	9
41	Constitutive soil model	11
42	Turbulent model	12
43	Frictional force for soil-structure interaction	12
44	Momentum and Energy exchange model	13
45	Solving momentum and energy exchange with an implicit solver	14
46	Equation of state for fluid phases	16
47	Numerical implementation	17
48	Interpolation from Solid Particle to Grid	18
49	Compute equation of state for fluid phase	20
50	Compute cell face velocity	20
51	Compute cell face temperature	21
52	Compute fluid pressure (implicit scheme)	22
53	Compute viscous shear stress term of the fluid phase	22
54	Compute nodal internal temperature of the solid phase	22
55	Compute and integrate acceleration of the solid phase	23
56	Compute Lagrangian value (mass, momentum and energy)	23
57	Compute Lagrangian specific volume of the fluid phase	24
58	Compute advection term and advance in time	25
59	Interpolate from cell to node of the solid phase	26
60	Update the particle variables	26
61	Numerical examples	27
62	Fluid Flow through isothermal porous media	27
63	Isothermal consolidation	28
64	Thermal induced cavity flow	29
65	Underwater debris flow	30
66	Validation of soil response to the seismic loading	34
67	Earthquake-induced submarine landslides	36

68	Conclusions	41
69	Acknowledgements	42
70	Appendix: Equation derivation	42
71	Evolution of porosity	42
72	Momentum conservation	43
73	Energy conservation	44
74	Advanced Fluid Pressure	45
75	Momentum and Energy exchange with an implicit solver	46

⁷⁶ **Nomenclature**

General variables

<u>Variable</u>	<u>Dimensions</u>	<u>Description</u>
V	$[L^3]$	Representative volume
n		Porosity
σ	$[ML^{-1}t^{-2}]$	Total stress tensor
Δt	$[t]$	Time increment
\mathbf{b}	$[ML^1t^{-2}]$	Body force
c_v	$[L^2t^{-2}T^{-1}]$	Constant volume specific heat
f_d	$[MLt^{-2}]$	Drag forces in momentum exchange term
f^{int}	$[MLt^{-2}]$	Internal forces
f^{ext}	$[MLt^{-2}]$	External forces
q_{fs}	$[MLt^{-2}]$	Heat exchange term
S		Weighting function
∇S		Gradient of weighting function

⁷⁷

Solid phase

<u>Variable</u>	<u>Dimensions</u>	<u>Description</u>
m_s	$[M]$	Solid mass
ρ_s	$[ML^{-3}]$	Solid density
ϕ_s		Solid volume fraction
$\bar{\rho}_s$	$[ML^{-3}]$	Bulk Solid density
\mathbf{x}_s	$[L]$	Solid Position vector
\mathbf{U}_s	$[Lt^{-1}]$	Solid Velocity vector
\mathbf{a}_s	$[Lt^{-2}]$	Solid Acceleration vector
σ'	$[ML^{-1}t^{-2}]$	Effective Stress tensor
ϵ		Strain tensor
e_s	$[L^2t^{-2}]$	Solid Internal energy per unit mass
T_s	$[T]$	Solid Temperature
\mathbf{F}_s		Solid Deformation gradient
V_s	$[L^3]$	Solid Volume

Fluid phase

<u>Variable</u>	<u>Dimensions</u>	<u>Description</u>
m_f	[M]	Fluid mass
ρ_f	[ML ⁻³]	Fluid density
ϕ_f		Fluid volume fraction
$\bar{\rho}_f$	[ML ⁻³]	Bulk Fluid density
\mathbf{U}_f	[Lt ⁻¹]	Fluid Velocity vector
$\boldsymbol{\sigma}_f$	[ML ⁻¹ t ⁻²]	Fluid stress tensor
p_f	[ML ⁻¹ t ⁻²]	Fluid isotropic pressure
$\boldsymbol{\tau}_f$	[ML ⁻¹ t ⁻²]	Fluid shear stress tensor
e_f	[L ² t ⁻²]	Fluid Internal energy per unit mass
T_f	[T]	Fluid Temperature
v_f	[L ³ /M]	Fluid Specific volume $\frac{1}{\rho_f}$
α_f	[1/T]	Thermal expansion
μ	[ML ⁻¹ t ⁻¹]	Fluid viscosity
V_f	[L ³]	Fluid Volume

Superscript

<u>Variable</u>	<u>Dimensions</u>	<u>Description</u>
n		Current time step
L		Lagrangian values
$n + 1$		Next time step

Subscript

c	Cell-centered quantity
p	Particle quantity
i	Node quantity
FC	Cell face quantity
L, R	Left and Right cell faces

79 **Introduction**

80 Many geological natural processes and their interactions with man-made
81 structures are influenced by soil-fluid-structure interactions. The prediction
82 of these processes requires a tool that can capture complex interactions
83 between soil, fluid, and structure, such as the process of submarine land-
84 slides. Indeed, The offshore infrastructure as well as coastal communities
85 may be vulnerable to submarine landslides. Submarine landslides contain
86 three stages: triggering, failure, and post-failure. Erosion or earthquakes can
87 trigger slope failures in the first stage. Following the failure, sediments move
88 quickly after the post-failure stage. In other words, solid-like sediments will
89 behave like a fluid after failure. This phase transition makes the simulation
90 of submarine landslides a challenging task.

91
92 Due to this phase transition, submarine landslide can be modeled by ei-
93 ther the Computational Fluid Dynamics (CFD) or the particle-based meth-
94 ods. For simulating submarine slides, CFD methods solve governing equa-
95 tions in a full-Eulerian framework [1, 2, 3, 4] with interface capturing tech-
96 niques. While CFD can handle complex flows (such as turbulent flows), it
97 cannot account for the triggering mechanism of submarine landslides because
98 it is not straightforward to consider 'soil constitutive laws' of sediment ma-
99 terials in the Eulerian framework. In contrast, particle-based methods can
100 overcome this problem by using the Lagrangian framework. These meth-
101 ods have been extensively used to simulate landslides, like Material Point
102 Method (MPM) [5], Smooth Particle Hydro Dynamics [6], Particle Finite
103 Element Method [7], or Coupled Eulerian Lagrangian Method [8]. For sim-
104 plicity, these simulations adopt total stress analysis which neglects the pore
105 pressure development which is key factor triggering slope failures.

106
107 Recent developments in particle-based methods model the coupling of
108 fluid flows in porous media by sets of Lagrangian particles. For the MPM
109 family, it is the double-point MPM ([9, 10, 11]) where fluid particles and
110 solid particles are overlapped in a single computational grid. Even if fluid
111 flows are considered, particle-based methods have numerical instability in
112 modeling the fluid flow, which requires additional numerical treatments such
113 as the B-bar method [9], null-space filter [12], or least square approximation
114 [13, 14]. Indeed, CFD is a more optimal option for complex fluid flows
115 especially dealing with large distortions of continuum fluid media. Therefore,

116 it could be ideal to combine the CFD with particle-based methods. More than
 117 50 particle-based methods have been developed to solve large deformations
 118 of solids over the last two decades [15], but the MPM appears to be the
 119 best candidate for coupling with the CFD. Because MPM incorporates a
 120 stationary mesh during computation, just like CFD. As such, both MPM
 121 and CFD can be coupled naturally in a unified computational mesh.



Figure 1: Interaction between soil-fluid-structure

122

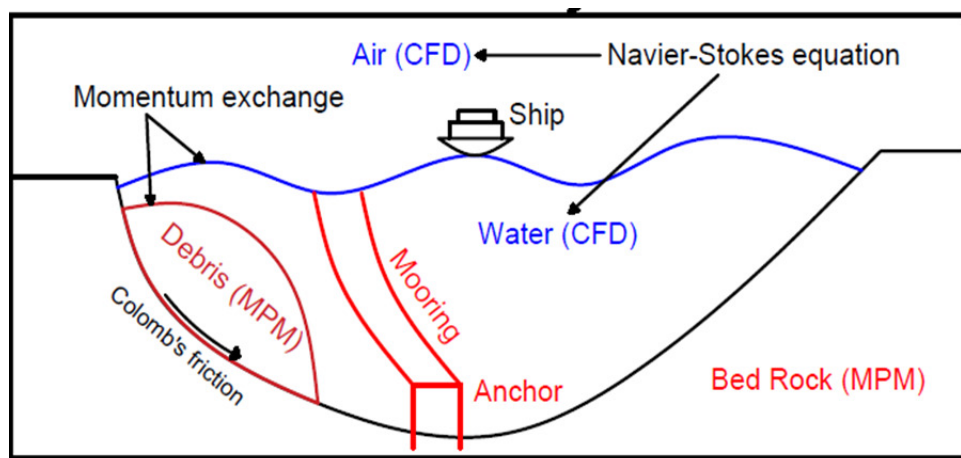


Figure 2: Coupling of soil-water-structure interaction using MPMICE

123 A numerical method for simulating soil-fluid-structure interaction (Figure
124 1) involving large deformations, is presented in this work in order to simu-
125 late the interaction between sediment (soil), seawater (fluid) and offshore
126 structures (structure) namely MPMICE (Figure 2). In the MPMICE, the
127 Material Point Method (MPM) is coupled with the Implicit Continuous Eu-
128 lerian (ICE). The MPM method is a particle method that allows the porous
129 soil to undergo arbitrary distortions. The ICE method, on the other hand,
130 is a conservative finite volume technique with all state variables located at
131 the cell center (temperature, velocity, mass, pressure). An initial technical
132 report [16] at Los Alamos National Laboratory provided the theoretical and
133 algorithmic foundation for the MPMICE, followed by the MPMICE devel-
134 opment and implementation in the high-performance Uintah computational
135 framework for simulating fluid-structure interactions [17]. This paper pri-
136 marily contributes further to the development of the MPMICE for analyzing
137 the **soil**-fluid-structure interaction, since sediment should be considered as a
138 porous media (soil) and not as a solid to capture the evolution of the pore
139 water pressure. Baumgarten et al. [18] made the first attempt at coupling
140 the Finite Volume Method with the MPM for the simulation of soil-fluid
141 interaction. In contrast to the mentioned work, we use implicit time inte-
142 gration for the multi phase flows instead of explicit time integration for the
143 single-phase flow.

144 **Theory and formulation**

145 This section lay out the theoretical framework for the MPMICE model.
146 We use the common notation of the continuum mechanics with vector and
147 tensor denoted simply by using bold font and scalar denoted by using normal
148 font. The notation are shown in Nomenclature.

149 *Assumptions*

150 The following assumptions are made for the MPMICE model.

- 151 1. Solid phases (MPM) are described in a Lagrangian formulation while
152 fluid phases (ICE) are described in an Eulerian formulation in the
153 framework of continuum mechanics and mixture theory.
- 154 2. Solid grains are incompressible while the fluid phases are compressible.
155 Solid's thermal expansion is negligible.
- 156 3. There is no mass exchange between solid and fluid phases.
- 157 4. Terzaghi's effective stress is valid.

158 *Governing equations*

159 A representative element volume Ω is decomposed by two domains: solid
160 domains Ω_s and fluid domains Ω_f . Then, all domains are homogenized
161 into two overlapping continua. Considering the volume fraction of solid
162 $\phi_s = \Omega_s/\Omega$ and fluid $\phi_f = \Omega_f/\Omega$ with the true (or Eulerian) porosity
163 $n = \sum \phi_f$ of the representative element volume, the average density of solid
164 and fluid phases are defined as:

165

$$\bar{\rho}_s = \phi_s \rho_s, \quad \bar{\rho}_f = \phi_f \rho_f \quad (1)$$

166 The mass of solid and fluid phases are:

167

$$m_s = \int_{\Omega_s} \rho_s dV = \bar{\rho}_s V, \quad m_f = \int_{\Omega_f} \rho_f dV = \bar{\rho}_f V \quad (2)$$

168 Reviewing the Terzaghi's effective stress concept for the saturated porous
169 media, the total stress $\boldsymbol{\sigma}$ is calculated by:

170

$$\boldsymbol{\sigma} = \boldsymbol{\sigma}' - p_f \mathbf{I} \quad (3)$$

171 The balance equations are derived based on the mixture theory. The rep-
172 resentative thermodynamic state of the fluid phases are given by the vector
173 $[m_f, \mathbf{U}_f, e_f, T_f, v_f]$ which are mass, velocity, internal energy, temperature,
174 specific volume. The representative state of the solid phases are given by the
175 vector $[m_s, \mathbf{U}_s, e_s, T_s, \boldsymbol{\sigma}', p_f]$ which are mass, velocity, internal energy, temper-
176 ature, effective stress and pore water pressure. The derivation is presented
177 in detail in the Appendix.

178

179 Mass Conservation

180 The mass balance equations for both fluid (e.g., water, air) and solid phases
181 are:

182

$$\frac{1}{V} \frac{\partial m_f}{\partial t} + \nabla \cdot (m_f \mathbf{U}_f) = 0, \quad \frac{1}{V} \frac{D_s m_s}{Dt} = 0 \quad (4)$$

183 Solving the mass balance equation of the solid phase leads to:

$$\frac{D_s n}{Dt} = \phi_s \nabla \cdot \mathbf{U}_s \quad (5)$$

184

185 Momentum Conservation

₁₈₆ The momentum balance equations for the fluid phases (e.g., water, air) are:

$$\frac{1}{V} \left[\frac{\partial(m_f \mathbf{U}_f)}{\partial t} + \nabla \cdot (m_f \mathbf{U}_f \mathbf{U}_f) \right] = -\phi_f \nabla p_f + \nabla \cdot \boldsymbol{\tau}_f + \bar{\rho}_f \mathbf{b} + \sum \mathbf{f}_d \quad (6)$$

₁₈₇ The momentum balance equations for the solid phases are:

$$\frac{1}{V} \frac{D_s(m_s \mathbf{U}_s)}{Dt} = \nabla \cdot (\boldsymbol{\sigma}') - \phi_s \nabla p_f + \bar{\rho}_s \mathbf{b} + \sum \mathbf{f}_{fric} - \sum \mathbf{f}_d \quad (7)$$

₁₈₈

₁₈₉ Energy Conservation

₁₉₀ The internal energy balance equations for the fluid phases (e.g., water, air)
₁₉₁ are:

$$\frac{1}{V} \left[\frac{\partial(m_f e_f)}{\partial t} + \nabla \cdot (m_f e_f \mathbf{U}_f) \right] = -\bar{\rho}_f p_f \frac{D_f v_f}{Dt} + \boldsymbol{\tau}_f : \nabla \mathbf{U}_f + \nabla \cdot \mathbf{q}_f + \sum q_{sf} \quad (8)$$

₁₉₂ The internal energy balance equations for the solid phase are:

$$\frac{m_s}{V} c_v \frac{D_s(T_s)}{Dt} = \boldsymbol{\sigma}' : \frac{D_s(\boldsymbol{\epsilon}_s^p)}{Dt} + \nabla \cdot \mathbf{q}_s - \sum q_{sf} \quad (9)$$

₁₉₃ where c_v is the specific heat at constant volume of the solid materials.

₁₉₄

₁₉₅ Closing the systems of equations, the following additional models are needed:

₁₉₆ (1) A constitutive equation to describe the stress - strain behaviour of solid
₁₉₇ phase (computing effective stress $\boldsymbol{\sigma}'$).

₁₉₈ (2) Optional turbulent model to compute the viscous shear stress $\boldsymbol{\tau}_f$.

₁₉₉ (3) Frictional forces \mathbf{f}_{fric} for the contact for soil-structure interaction be-
₂₀₀ tween solid/porous materials with the friction coefficient μ_{fric} .

₂₀₁ (4) Exchange momentum models (computing drag force \mathbf{f}_d) for interaction
₂₀₂ between materials.

₂₀₃ (5) Energy exchange models (computing temerature exhangre term q_{sf}) for
₂₀₄ interaction between materials.

₂₀₅ (6) An equation of state to establish relations between thermodynamics vari-
₂₀₆ ables of each fluid materials $[P_f, \bar{\rho}_f, v_f, T_f, e_f]$.

²⁰⁷ Four thermodynamic relations for the equation of states are:

$$\begin{aligned} e_f &= e_f(T_f, v_f) \\ P_f &= P_f(T_f, v_f) \\ \phi_f &= v_f \bar{\rho}_f \\ 0 &= n - \sum_{f=1}^{N_f} v_f \bar{\rho}_f \end{aligned} \quad (10)$$

²⁰⁸ *Constitutive soil model*

²⁰⁹ As a result of the explicit MPM formulation, we can derive the consti-
²¹⁰ tutive law in the updated Lagrangian framework of "small strain - large
²¹¹ deformation". Therefore, the rotation of the particles (representative ele-
²¹² ment volume) is manipulated by rotating the Cauchy stress tensor. First,
²¹³ the deformation gradient is decomposed into the polar rotation tensor \mathbf{R}_s^{n+1}
²¹⁴ and stretch tensor \mathbf{V}_s^{n+1} as:

$$\mathbf{F}_s^{n+1} = \mathbf{V}_s^{n+1} \mathbf{R}_s^{n+1} \quad (11)$$

²¹⁵ Then, before calling the constitutive model, the stress and strain rate tensor
²¹⁶ are rotated to the reference configuration as:

$$\boldsymbol{\sigma}'^{n*} = (\mathbf{R}_s^{n+1})^T \boldsymbol{\sigma}'^n \mathbf{R}_s^{n+1} \quad (12)$$

$$\delta\boldsymbol{\epsilon}^{n*} = (\mathbf{R}_s^{n+1})^T \delta\boldsymbol{\epsilon}^n \mathbf{R}_s^{n+1} \quad (13)$$

²¹⁸ Using the constitutive model with the input tensors $\boldsymbol{\sigma}'^{n*}, \delta\boldsymbol{\epsilon}^{n*}$ to compute
²¹⁹ the Cauchy stress tensor at the advanced time step $\boldsymbol{\sigma}'^{n+1*}$ then rotating it
²²⁰ back to current configuration as:

$$\boldsymbol{\sigma}'^{n+1} = \mathbf{R}_s^{n+1} \boldsymbol{\sigma}'^{n+1*} (\mathbf{R}_s^{n+1})^T \quad (14)$$

²²¹ In this paper, we adopt the hyper-elastic Neo Hookean model for the structure
²²² materials and additionally Mohr-Coulomb failure criteria for the soil (porous
²²³ media) materials. The Cauchy stress of the hyper-elastic Neo Hookean model
²²⁴ can be written as:

$$\boldsymbol{\sigma}' = \frac{\lambda \ln(J)}{J} + \frac{\mu}{J} (\mathbf{F} \mathbf{F}^T - \mathbf{J}) \quad (15)$$

²²⁵ where λ and μ are bulk and shear modulus ad J is the determinant of the
²²⁶ deformation gradient \mathbf{F} . And the yield function f and flow potentials g of

²²⁷ the Mohr-Coulomb can be written as:

$$\begin{aligned} f &= -\sigma'_1 + \sigma'_3 + 2c' \cos(\phi') + (\sigma'_1 + \sigma'_3) \sin(\phi') \\ g &= -\sigma'_1 + \sigma'_3 + 2c' \cos(\psi') + (\sigma'_1 + \sigma'_3) \sin(\psi') \end{aligned} \quad (16)$$

²²⁸ In the equations, c' , ϕ' , and ψ' represent the cohesion, friction angle, and
²²⁹ dilation angle, respectively. σ'_1 and σ'_3 denote the maximum and minimum
²³⁰ principal stresses, with the condition $\sigma'_1 < \sigma'_3 < 0$. It is important to note
²³¹ that in our assumptions, stress is considered positive during extension, which
²³² means the signs of the stresses in these equations are opposite to those in
²³³ standard Soil Mechanic's textbooks.

²³⁴ *Turbulent model*

²³⁵ The turbulent effect is modelled using a statistical approach namely large-
²³⁶ eddy simulation. In this approach, the micro-scale turbulent influence in the
²³⁷ dynamics of the macro-scale motion is computed through simple models like
²³⁸ Smagorinsky model. In the Smagorinsky model, the residual stress tensor is:

$$\tau_{ij} = 2\mu_{eff}(\bar{S}_{ij} - \frac{1}{3}\delta_{ij}\bar{S}_{kk}) + \frac{1}{3}\delta_{ij}\tau_{kk} \quad (17)$$

²³⁹ where the strain rate tensor is given by:

$$\bar{S}_{ij} = \frac{1}{2}(\frac{\delta \bar{U}_i}{\delta x_j} + \frac{\delta \bar{U}_j}{\delta x_i}) \quad (18)$$

²⁴⁰ and the effective viscosity is sum of molecular viscosity and turbulent viscos-
²⁴¹ ity $\mu_{eff} = \mu + \mu_t$ in which the turbulent viscosity μ_t is calculated by:

$$\mu_t = (C_s \Delta)^2 \sqrt{2\bar{S}_{ij}\bar{S}_{ij}} \quad (19)$$

²⁴² where C_s is the Smagorinsky constant with the value of 0.1 and $\Delta = \sqrt[3]{dxdydz}$
²⁴³ is the grid size that defines the subgrid length scale.

²⁴⁴ *Frictional force for soil-structure interaction*

²⁴⁵ MPMICE includes a contact law for the interaction between soil and
²⁴⁶ structure using the first Coulomb friction contact for MPM presented by
²⁴⁷ Bardenhagen et al. ([19]). The magnitude of the friction force at the contact
²⁴⁸ depends on the friction coefficient μ_{fric} and the normal force \mathbf{f}_{norm} computed
²⁴⁹ from the projection of the contact force in the normal direction.

$$\mathbf{f}_{fric} = \mu_{fric} \mathbf{f}_{norm} \quad (20)$$

250 The contact determines whether the soil is sliding or sticking to the structure
 251 by comparing the friction force with the sticking force \mathbf{f}_{stick} computed from
 252 the projection of the contact force in the tangent direction as:

$$\begin{aligned} \text{if } \mathbf{f}_{fric} \geq \mathbf{f}_{stick} & \text{ no sliding} \\ \text{if } \mathbf{f}_{fric} < \mathbf{f}_{stick} & \text{ sliding occurs} \end{aligned} \quad (21)$$

253 Frictional sliding between solid materials also generates dissipation and the
 254 work rate generated from the sliding can be calculated as:

$$\Delta W_{friction} = \mathbf{f}_{fric} d \quad (22)$$

255 where d is the sliding distance which can be computed based on the sliding
 256 velocity between two materials.

257 *Momentum and Energy exchange model*

258 Currently, the energy exchange coefficient H_{sf} is assumed to be constant
 259 for the sake of simplicity. Then the energy exchange can be written as:

$$q_{sf} = H_{sf}(T_f - T_s) \quad (23)$$

260 On the other hand, the drag force can be calculated as:

$$f_d = K(\mathbf{U}_s - \mathbf{U}_f) \quad (24)$$

261 For the momentum exchange between fluid flows and porous media, we as-
 262 sume that the drag force \mathbf{f}_d depends on the average grain size of the grains
 263 D_p , the porosity n , the fluid viscosity μ_f , and is proportional to the relative
 264 velocities of soil grains and fluid $(\mathbf{U}_s - \mathbf{U}_f)$. Based on recent investigation
 265 of CFD simulations of fluid flow around mono- and bi-disperse packing of
 266 spheres for $0.1 < \phi_s < 0.6$ and $Re < 1000$ [20]. The drag force is given by:
 267

$$\mathbf{f}_d = \frac{18\phi_s(1-\phi_s)\mu_f}{D_p^2} F(\phi_s, Re)(\mathbf{U}_s - \mathbf{U}_f) \quad (25)$$

268 where Reynolds number Re are computed as:

$$Re = \frac{n\rho_f D_p}{\mu_f} \|(\mathbf{U}_s - \mathbf{U}_f)\| \quad (26)$$

²⁶⁹ The function $F(\phi_s, Re)$ can be calculated as:

$$F(\phi_s, Re) = F(\phi_s, 0) + \frac{0.413Re}{24(1 - \phi_s)^2} \left(\frac{(1 - \phi_s)^{-1} + 3\phi_s(1 - \phi_s) + 8.4Re^{-0.343}}{1 + 10^{3\phi_s}Re^{-(1+4\phi_s)/2}} \right) \quad (27)$$

²⁷⁰ where the low Reynold coefficient $F(\phi_s, Re \rightarrow 0)$ is:

$$F(\phi_s, 0) = \frac{10\phi_s}{(1 - \phi_s)^2} + (1 - \phi_s)^2(1 + 1.5\sqrt{\phi_s}) \quad (28)$$

²⁷¹ When validating the model with analytical solution, it requires to know the
²⁷² hydraulic conductivity K . In such case, we convert the equation (25) to
²⁷³ Kozeny-Carman formula by assuming $F(\phi_s, Re) = 10\phi_s/(1 - \phi_s)^2$, leading to

$$\mathbf{f}_d = \frac{180\phi_s^2\mu_f}{D_p^2(1 - \phi_s)} (\mathbf{U}_s - \mathbf{U}_f) \quad (29)$$

²⁷⁴ Then, the draging force following the Darcy law is given by:

$$\mathbf{f}_d = \frac{n^2\mu_f}{\kappa} (\mathbf{U}_s - \mathbf{U}_f) \quad (30)$$

²⁷⁵ where κ being intrinsic permeability of soil which can be written as:

$$\kappa = \frac{K\mu_f}{\rho_f g} \quad (31)$$

²⁷⁶ As such, the hydraulic conductivity will be expressed as:

$$K = \frac{D_p^2(1 - \phi_s)^3}{180\phi_s^2\mu_f} \rho_f g \quad (32)$$

²⁷⁷ *Solving momentum and energy exchange with an implicit solver*

²⁷⁸ The derivation of the implicit integration for the momentum exchange is
²⁷⁹ presented in the Appendix's section 'Momentum and energy exchange with
²⁸⁰ an implicit solver'. The linear equations for multi phases i,j=1:N has the
²⁸¹ form as:

$$\begin{vmatrix} (1 + \beta_{ij}) & -\beta_{ij} \\ -\beta_{ji} & (1 + \beta_{ji}) \end{vmatrix} \begin{vmatrix} \Delta\mathbf{U}_i \\ \Delta\mathbf{U}_j \end{vmatrix} = \begin{vmatrix} \beta_{ij}(\mathbf{U}_i^* - \mathbf{U}_j^*) \\ \beta_{ji}(\mathbf{U}_i^* - \mathbf{U}_j^*) \end{vmatrix}$$

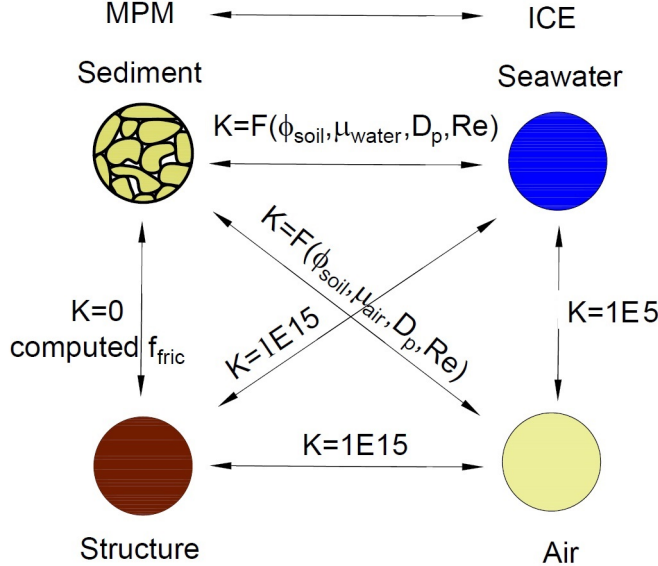


Figure 3: Momentum exchange coefficient between materials

282 where the intermediate velocity for fluid phases $f=1:N_f$ and for solid/porous
 283 phases $s=1:N_s$ can be calculated by:

$$\begin{aligned} U_f^* &= U_f^n + \Delta t \left(-\frac{\nabla P_f^{n+1}}{\rho_f^n} + \frac{\nabla \cdot \tau_f^n}{\bar{\rho}_f^n} + \mathbf{b} \right) \\ U_s^* &= U_s^n + \Delta t \left(\frac{\nabla \cdot \sigma'^n}{\bar{\rho}_s^n} - \frac{\nabla P_f^{n+1}}{\rho_s} + \mathbf{b} \right) \end{aligned} \quad (33)$$

284 Also, the momentum exchange coefficient can be computed at every time
 285 step as $\beta_{12} = K/\bar{\rho}_f^n$ and $\beta_{21} = K/\bar{\rho}_s^n$ with the coefficient depending on the
 286 different type of interactions (see Figure 3) as for example:

287

- 288 1. The drag force is set to zero in soil-structure interactions, and instead
 289 the frictional force is computed.
- 290 2. As a result of fluid-structure interaction, the momentum exchange coef-
 291 ficient should be extremely high (1E15) when the solid material points
 292 are considered to be zero-porosity/zero-permeability.
- 293 3. In the case of soil-fluid interaction, the drag force is calculated using
 294 the equation (25). Considering that air has a much lower viscosity than

water, its drag force is much lower than the drag force of water in a pore.

4. A momentum exchange coefficient of 1E5 is applied between multiphase flows. This value is far higher than reality [21], but it is necessary to have enough numerical stability to conduct simulations in the numerical example.

Similar approach applied for the energy exchange term leading to:

$$\begin{vmatrix} (1 + \eta_{ij}) & -\eta_{ij} \\ -\eta_{ji} & (1 + \eta_{ji}) \end{vmatrix} \begin{vmatrix} \Delta T_i \\ \Delta T_j \end{vmatrix} = \begin{vmatrix} \eta_{ij}(T_i^n - T_j^n) \\ \eta_{ji}(T_j^n - T_i^n) \end{vmatrix}$$

with η being the energy exchange coefficient.

Equation of state for fluid phases

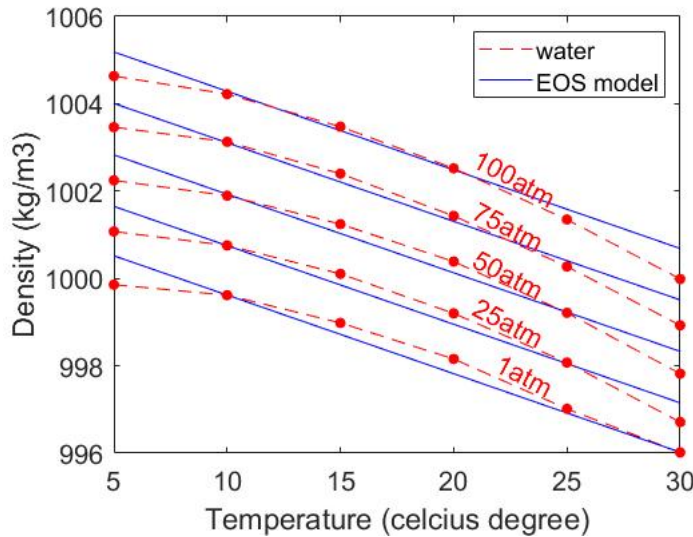


Figure 4: Equation of state of water

The equation of state establishes relations between thermodynamics variables $[P_f, \rho_f, T_f]$. The choice of the equation of state depends on the types of the fluid materials. For example, for the air, it is possible to assume the equation of state for the perfect gas which obeys:

$$P_f = \rho_f R T_f \quad (34)$$

308 where R is the gas constant. For the water, a simple linear equation of state
 309 is in the following form:

$$P_f = P_{ref} + K_f(\rho_f - \rho_{ref} + \alpha_f(T_f - T_{ref})) \quad (35)$$

310 where reference pressure $P_{ref} = 1$ atm = 101325 Pa, reference temperature
 311 $T_{ref} = 10^\circ\text{C}$, reference density $\rho_{ref} = 999.8 \text{ kg/m}^3$, the bulk modulus of water
 312 $K_f = 2 \text{ GPa}$, and the water thermal expansion $\alpha_f = 0.18 \text{ }^\circ\text{C}^{-1}$. Equation
 313 (35) matches well with the state of the water (see Figure 4).

314 **Numerical implementation**

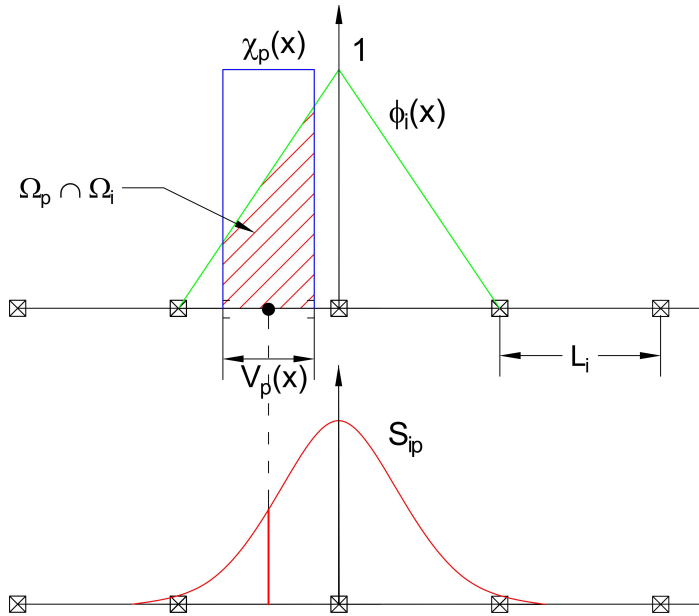


Figure 5: GIMP weighting function (red as a convolution of the linear basis shape function (green) and the characteristic function (blue))

315 The fluid phases are discretized in the grid with the state variables stored
 316 at the centroid of the cells $[\rho_{f,c}, \mathbf{U}_{f,c}, T_{f,c}, v_{f,c}]$ while the solid phase is dis-
 317 cretized in the particles with the state variables $[m_{sp}, \mathbf{U}_{sp}, T_{sp}, \boldsymbol{\sigma}'_{sp}]$. In the
 318 Material Point Method, we use the generalized interpolation technique [22]
 319 using the weight function as a convolution of a grid shape function $N_i(\mathbf{x})$ in

³²⁰ a nodal domain Ω_i and a characteristic function $\chi_p(\mathbf{x})$ in a particle domain
³²¹ Ω_p with the volume $V_p(\mathbf{x})$ as follows:

$$S_{ip} = \frac{1}{V_p} \int_{\Omega_i \cap \Omega_p} N_i(\mathbf{x}) \chi_p(\mathbf{x}) d\mathbf{x} \quad (36)$$

³²² where the volume $V_p(\mathbf{x})$ of the material point p can be calculated as:

$$V_p = \int_{\Omega_p} \chi_p(\mathbf{x}) d\mathbf{x} \quad (37)$$

³²³ The characteristic function is the Heaviside function as $\chi_p = 1$ if $\mathbf{x} \in \Omega_p$,
³²⁴ otherwise 0 (see Figure 5). For the interpolation of the centroid of the cell,
³²⁵ the linear basis function is used as:

$$S_{ci} = N_i(\mathbf{x}_c) \quad (38)$$

³²⁶ The time discretization are solved using the following steps.

³²⁷ *Interpolation from Solid Particle to Grid*

³²⁸ The nodal values of the solid state (mass, velocity, temperature, volume)
³²⁹ are:

$$\begin{aligned} m_{si}^n &= \sum S_{ip} m_{sp} \\ \mathbf{U}_{si}^n &= \frac{\sum S_{ip} (m\mathbf{U})_{sp}^n}{m_{si}^n} \\ T_{si}^n &= \frac{\sum S_{ip} (mT)_{sp}^n}{m_{si}^n} \\ V_{si}^n &= \frac{\sum S_{ip} (mV)_{sp}^n}{m_{si}^n} \\ \boldsymbol{\sigma}_{si}^n &= \frac{\sum S_{ip} (\boldsymbol{\sigma}V)_{sp}^n}{V_{si}^n} \end{aligned} \quad (39)$$

³³⁰ The nodal internal forces is calculated by:

$$\mathbf{f}_{si}^{int,n} = - \sum \nabla S_{ip} (\boldsymbol{\sigma}'_{sp})^n V_{sp}^n \quad (40)$$

³³¹ The nodal external forces $f_{si}^{ext,n}$ and the frictional forces from soil-structure
³³² interaction $f_{fric,si}^n$ from contact between materials are computed here.

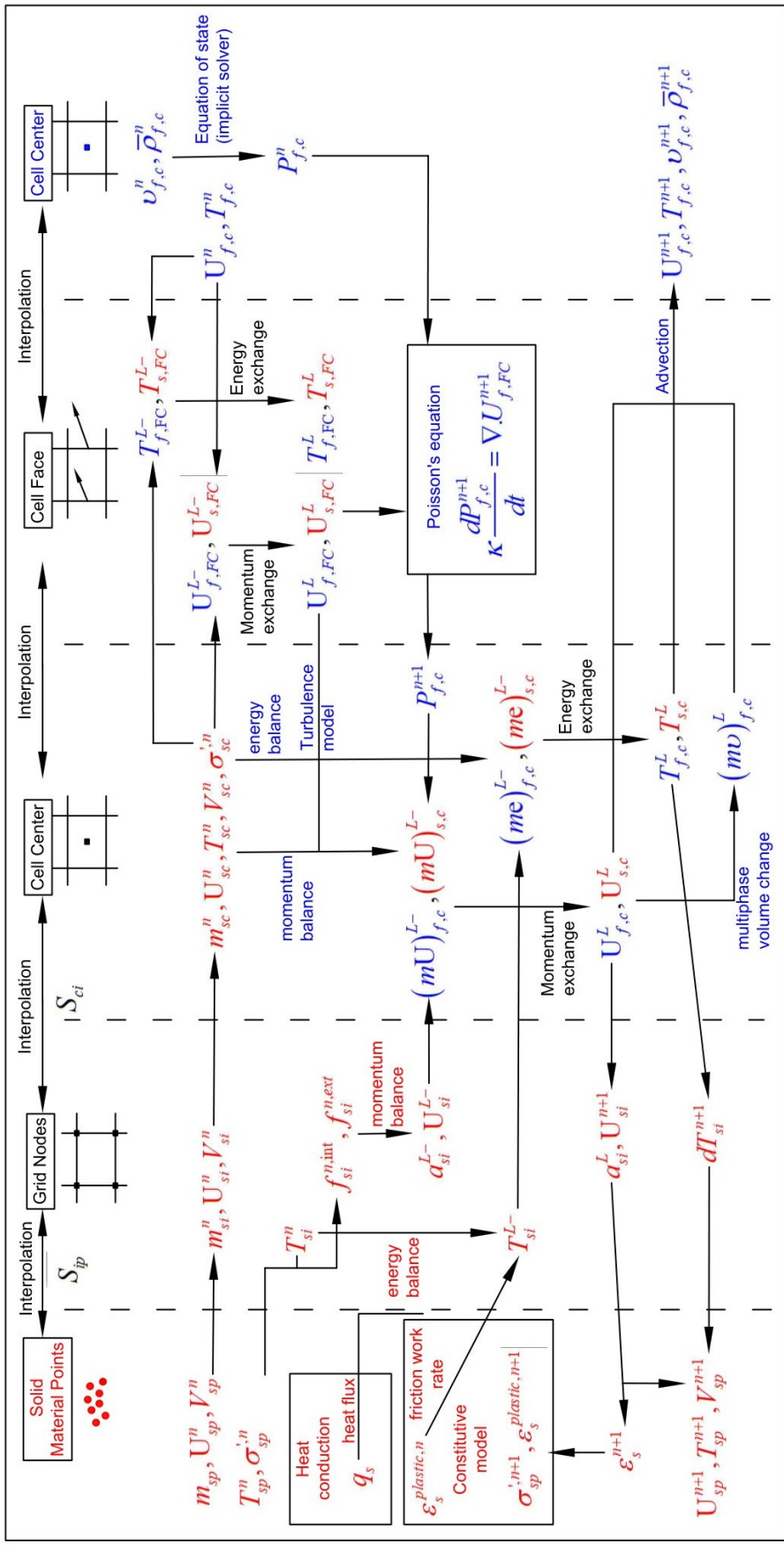


Figure 6: Numerical implementation of MPMICE

³³³ Then we compute the solid cell variables as:

$$\begin{aligned}
 m_{sc}^n &= \sum S_{ci} m_{si} \\
 \rho_{sc}^n &= \frac{m_{sc}^n}{V} \\
 \mathbf{U}_{sc}^n &= \sum S_{ci} \mathbf{U}_{si}^n \\
 T_{sc}^n &= \sum S_{ci} T_{si}^n \\
 V_{sc}^n &= \sum S_{ci} V_{si}^n \\
 \boldsymbol{\sigma}_{sc}^n &= \sum S_{ci} \boldsymbol{\sigma}_{si}^n
 \end{aligned} \tag{41}$$

³³⁴ *Compute equation of state for fluid phase*

³³⁵ The total fluid material volume of a cell is:

$$V_{total} = \sum_{f=1}^{N_f} M_f v_f \tag{42}$$

³³⁶ We need to find $P_{f,c}^n$ which allows each fluid materials obey their equation of
³³⁷ states $[P_f, \rho_f, v_f, T_f, e_f]$ but also allow mass of all fluid materials to fill the
³³⁸ entire the pore volume without ongoing compression or expansion following
³³⁹ the condition as follows:

$$0 = n - \sum_{f=1}^{N_f} v_f \bar{\rho}_f \tag{43}$$

³⁴⁰ Then, we can use the Newton-Raphson interation to find the value of $P_{f,c}^n$
³⁴¹ which satisfies the equation (42, 43) and each equation of states of each fluid
³⁴² materials.

³⁴³ *Compute cell face velocity*

³⁴⁴ Following the derivation in the Appendix: Advanced Fluid Pressure, we
³⁴⁵ first compute the fluid cell face velocity as:

$$\mathbf{U}_{f,FC}^{L-} = \frac{(\bar{\rho} \mathbf{U})_{f,FC}^n}{\bar{\rho}_{f,FC}^n} + \Delta t \left(-\frac{\nabla^{FC} P_{f,c}^n}{\bar{\rho}_{f,FC}^n} + \frac{\nabla^{FC} \cdot \boldsymbol{\tau}^n}{\bar{\rho}_{s,FC}} + \mathbf{b} \right) \tag{44}$$

³⁴⁶ The equation (44) is discretized in three dimension (noted that $\nabla^{FC} \cdot \boldsymbol{\tau} = 0$),
³⁴⁷ for example the discretized equation in the x direction is:

$$U_{fx}^{L-} = \frac{(\bar{\rho} U)_{fx,R}^n + (\bar{\rho} U)_{fx,L}^n}{\bar{\rho}_{fx,L}^n + \bar{\rho}_{fx,R}^n} + \Delta t \left(-\frac{2(v_{fx,L}^n v_{fx,R}^n)}{v_{fx,L}^n + v_{fx,R}^n} \frac{P_{f,cx,R}^n - P_{f,cx,L}^n}{\Delta x} + b_x \right) \tag{45}$$

³⁴⁸ The cell face solid velocity can be calculated as:

$$\mathbf{U}_{s,FC}^{L-} = \frac{(\bar{\rho}\mathbf{U})_{s,FC}^n}{\bar{\rho}_{s,FC}^n} + \Delta t \left(\frac{\nabla^{FC} \cdot \boldsymbol{\sigma}_c'^n}{\bar{\rho}_{s,FC}} - \frac{\nabla^{FC} P_{f,c}^n}{\rho_s} + \mathbf{b} \right) \quad (46)$$

³⁴⁹ The equation (46) is discretized in three dimension (noted that $\nabla^{FC} \cdot \boldsymbol{\sigma}_{ij} = 0$
³⁵⁰ with $i \neq j$), for example the discretized equation in the x direction is:

$$U_{sx}^{L-} = \frac{(\bar{\rho}U)_{sx,R}^n + (\bar{\rho}U)_{sx,L}^n}{\bar{\rho}_{sx,L}^n + \bar{\rho}_{sx,R}^n} + \Delta t \left(\frac{2(\sigma_{xx,R} - \sigma_{xx,L})}{(\bar{\rho}_{sx,L}^n + \bar{\rho}_{sx,R}^n)\Delta x} - \frac{P_{f,cx,R}^n - P_{f,cx,L}^n}{\rho_s \Delta x} + b_x \right) \quad (47)$$

³⁵¹ Then, we compute the modified cell face velocity \mathbf{U}_{FC}^L considering the mo-
³⁵² mentum exchange (see the Appendix: Momentum exchange with an implicit
³⁵³ solve) as follows:

$$\begin{aligned} \mathbf{U}_{f,FC}^L &= \mathbf{U}_{f,FC}^{L-} + \Delta \mathbf{U}_{f,FC} \\ \mathbf{U}_{s,FC}^L &= \mathbf{U}_{s,FC}^{L-} + \Delta \mathbf{U}_{s,FC} \end{aligned} \quad (48)$$

³⁵⁴ The linear equation below is solved to obtain the increment of velocity with
³⁵⁵ $i,j = 1 : N$ as:

$$\begin{vmatrix} (1 + \beta_{ij}) & -\beta_{ij} \\ -\beta_{ji} & (1 + \beta_{ji}) \end{vmatrix} \begin{vmatrix} \Delta \mathbf{U}_{i,FC} \\ \Delta \mathbf{U}_{j,FC} \end{vmatrix} = \begin{vmatrix} \beta_{ij}(\mathbf{U}_{i,FC}^{L-} - \mathbf{U}_{j,FC}^{L-}) \\ \beta_{ji}(\mathbf{U}_{j,FC}^{L-} - \mathbf{U}_{i,FC}^{L-}) \end{vmatrix}$$

³⁵⁶ Compute cell face temperature

³⁵⁷ Similar to the velocity, the faced temperature is computed, for example
³⁵⁸ in x direction, as:

$$\begin{aligned} T_{fx}^{L-} &= \frac{(\bar{\rho}T)_{fx,R}^n + (\bar{\rho}T)_{fx,L}^n}{\bar{\rho}_{fx,L}^n + \bar{\rho}_{fx,R}^n} \\ T_{sx}^{L-} &= \frac{(\bar{\rho}T)_{sx,R}^n + (\bar{\rho}T)_{sx,L}^n}{\bar{\rho}_{sx,L}^n + \bar{\rho}_{sx,R}^n} \end{aligned} \quad (49)$$

³⁵⁹ Then, we compute the modified cell face temperature T_{FC}^L considering the
³⁶⁰ energy exchange (see the Appendix: Momentum and energy exchange with
³⁶¹ an implicit solver) as follows:

$$\begin{aligned} T_{f,FC}^L &= T_{f,FC}^{L-} + \Delta T_{f,FC} \\ T_{s,FC}^L &= T_{s,FC}^{L-} + \Delta T_{s,FC} \end{aligned} \quad (50)$$

³⁶² The linear equation below is solved to determine the increment of velocity
³⁶³ with $i,j = 1 : N$ as:

$$\begin{vmatrix} (1 + \eta_{ij}) & -\eta_{ij} \\ -\eta_{ji} & (1 + \eta_{ji}) \end{vmatrix} \begin{vmatrix} \Delta T_{i,FC} \\ \Delta T_{j,FC} \end{vmatrix} = \begin{vmatrix} \eta_{ij}(T_{i,FC}^{L-} - T_{j,FC}^{L-}) \\ \eta_{ji}(T_{j,FC}^{L-} - T_{i,FC}^{L-}) \end{vmatrix}$$

364 ***Compute fluid pressure (implicit scheme)***

365 For single phase flow, the increment of the fluid pressure can be computed
366 as:

$$\kappa_f \frac{\Delta P}{dt} = \nabla^c \cdot \mathbf{U}_{f,FC}^{n+1} \quad (51)$$

367 For multi-phase flows, the increment of the fluid pressure of the mixture can
368 be computed as:

$$\kappa \frac{\Delta P}{dt} = \sum_{f=1}^{N_f} \nabla^c \cdot (\phi_{f,FC} \mathbf{U}_{f,FC})^{n+1} \quad (52)$$

369 where $\kappa = \sum_{f=1}^{N_f} (\phi_{f,FC} \kappa_f) / \sum_{f=1}^{N_f} (\phi_{f,FC})$. Then, the fluid pressure at cell
370 center is:

$$P_c^{n+1} = P_c^n + \Delta P_c^n \quad (53)$$

371 Finally, the cell face advanced fluid pressure is:

$$P_{FC}^{n+1} = \left(\frac{P_{c,L}^{n+1}}{\bar{\rho}_{f,L}^n} + \frac{P_{c,R}^{n+1}}{\bar{\rho}_{f,R}^n} \right) / \left(\frac{1}{\bar{\rho}_{f,L}^n} + \frac{1}{\bar{\rho}_{f,R}^n} \right) = \left(\frac{P_{c,L}^{n+1} \bar{\rho}_{f,R}^n + P_{c,R}^{n+1} \bar{\rho}_{f,L}^n}{\bar{\rho}_{f,L}^n \bar{\rho}_{f,R}^n} \right) \quad (54)$$

372 ***Compute viscous shear stress term of the fluid phase***

373 This part compute the viscous shear stress $\Delta(m\mathbf{U})_{f,c,\tau}$ for a single vis-
374 cous compressible Newtonian fluid and optionally shear stress induced by the
375 turbulent model.

376 ***Compute nodal internal temperature of the solid phase***

377 The nodal internal temperature rate is computed based on the heat con-
378 duction model as below:

$$dT_{si}^{L-} = \frac{(\Delta W_{si}^n + \Delta W_{fric,i}^n + \nabla^i \cdot \mathbf{q}_{si}^n)}{m_{si}^n c_v} \quad (55)$$

379 where $\Delta W_{si}^n = \boldsymbol{\sigma}' : \frac{D_s(\boldsymbol{\epsilon}_s^p)}{Dt}$ is the mechanical work rate computed from the
380 constitutive model with $\boldsymbol{\epsilon}_s^p$ is the plastic strain, $\Delta W_{fric,i}^n$ is the work rate
381 computed from the contact law due to the frictional sliding between solid
382 materials. The heat flux is $\mathbf{q}_s = \bar{\rho}_s \beta_s \nabla T_s$ with β_s being the thermal conduc-
383 tivity of the solid materials.

$$T_{si}^{L-} = T_{si}^n + dT_{si}^{L-} \quad (56)$$

384 ***Compute and integrate acceleration of the solid phase***

385 After interpolating from material points to the nodes, the nodal acceleration
386 and velocity are calculated by:

$$\mathbf{a}_{si}^{L-} = \frac{\mathbf{f}_{si}^{int,n} + \mathbf{f}_{si}^{ext,n}}{m_{si}^n} + \mathbf{g} \quad (57)$$

387 $\mathbf{U}_{si}^{L-} = \mathbf{U}_{si}^n + \mathbf{a}_{si}^{L-} \Delta t \quad (58)$

388 ***Compute Lagrangian value (mass, momentum and energy)***

389 For the fluid phase, the linear momentum rate, the energy rate are:

$$\Delta(m\mathbf{U})_{f,c} = Vn_c^n \nabla^c P_c^{n+1} + \Delta(m\mathbf{U})_{f,c,\tau} + V\bar{\rho}_{f,c}^n g \quad (59)$$

390 $\Delta(me)_{f,c} = Vn_c^n P_c^{n+1} \nabla^c \cdot \mathbf{U}_{f,FC}^* + \nabla^c \cdot \mathbf{q}_{f,c}^n \quad (60)$

391 The Lagrangian value of the mass, linear momentum and energy of fluid
392 phases without momentum exchange are:

393 $m_{f,c}^L = V\bar{\rho}_{f,c}^n \quad (61)$

394 $(m\mathbf{U})_{f,c}^{L-} = V\bar{\rho}_{f,c}^n \mathbf{U}_{f,c}^n + \Delta(m\mathbf{U})_{f,c} \quad (62)$

395 $(me)_{f,c}^{L-} = V\bar{\rho}_{f,c}^n T_{f,c}^n c_v + \Delta(me)_{f,c} \quad (63)$

396 For the solid phase, the Lagrangian value of the linear momentum and energy
397 of solid phase are:

398 $m_{sc}^L = m_{sc}^n \quad (64)$

399 $(m\mathbf{U})_{sc}^{L-} = \sum S_{ci} m_{si}^n \mathbf{U}_{si}^{L-} + V(1 - n_c^n) \nabla^c P_{f,c}^{n+1} \quad (65)$

400 $(me)_{sc}^{L-} = \sum S_{ci} m_{si}^n T_{si}^L c_v \quad (66)$

401 To consider the momentum exchange, the Lagrangian velocity is modified as:

$$\begin{aligned} \mathbf{U}_{f,c}^L &= \mathbf{U}_{f,c}^{L-} + \Delta\mathbf{U}_{f,c} \\ \mathbf{U}_{sc}^L &= \mathbf{U}_{sc}^{L-} + \Delta\mathbf{U}_{sc} \end{aligned} \quad (67)$$

402 where the cell-centered intermediate velocity can be calculated by:

$$\begin{aligned} \mathbf{U}_{f,c}^{L-} &= \frac{(m\mathbf{U})_{f,c}^{L-}}{m_{f,c}^L} \\ \mathbf{U}_{sc}^{L-} &= \frac{(m\mathbf{U})_{sc}^{L-}}{m_{sc}^L} \end{aligned} \quad (68)$$

⁴⁰¹ And the increment of the velocity $\mathbf{U}_{f,c}$, $\Delta\mathbf{U}_{sc}$ can be computed by solving
⁴⁰² the linear equation with $i,j = 1:N$ as:

$$\begin{vmatrix} (1 + \beta_{ij}) & -\beta_{ij} \\ -\beta_{ji} & (1 + \beta_{ji}) \end{vmatrix} \begin{vmatrix} \Delta\mathbf{U}_{i,c} \\ \Delta\mathbf{U}_{j,c} \end{vmatrix} = \begin{vmatrix} \beta_{ij}(\mathbf{U}_{i,c}^{L-} - \mathbf{U}_{j,c}^{L-}) \\ \beta_{ji}(\mathbf{U}_{j,c}^{L-} - \mathbf{U}_{i,c}^{L-}) \end{vmatrix}$$

⁴⁰³ To consider the energy exchange, the Lagrangian temperature is modified as:

$$\begin{aligned} T_{f,c}^L &= T_{f,c}^{L-} + \Delta T_{f,c} \\ T_{sc}^L &= T_{sc}^{L-} + \Delta T_{sc} \end{aligned} \quad (69)$$

⁴⁰⁴ where the cell-centered intermediate temperature can be calculated by:

$$\begin{aligned} T_{f,c}^{L-} &= \frac{(mT)_{f,c}^{L-}}{m_{f,c}^L c_v} \\ T_{sc}^{L-} &= \frac{(mT)_{sc}^{L-}}{m_{sc}^L c_v} \end{aligned} \quad (70)$$

⁴⁰⁵ And the increment of the velocity can be computed by solving the linear
⁴⁰⁶ equation with $i,j = 1:N$ as:

$$\begin{vmatrix} (1 + \eta_{ij}) & -\eta_{ij} \\ -\eta_{ji} & (1 + \eta_{ji}) \end{vmatrix} \begin{vmatrix} \Delta T_{i,c} \\ \Delta T_{j,c} \end{vmatrix} = \begin{vmatrix} \eta_{ij}(T_{i,c}^{L-} - T_{j,c}^{L-}) \\ \eta_{ji}(T_{j,c}^{L-} - T_{i,c}^{L-}) \end{vmatrix}$$

⁴⁰⁷ Finally, we obtain the cell-centered solid acceleration and temperature rate
⁴⁰⁸ as:

$$d\mathbf{U}_{sc}^L = \frac{(m\mathbf{U})_{sc}^L - (m\mathbf{U})_{sc}^n}{m_{sc}^L \Delta t} \quad (71)$$

$$dT_{sc}^L = \frac{(me)_{sc}^L - (me)_{sc}^n}{m_{sc}^L c_v \Delta t} \quad (72)$$

⁴¹⁰ Compute Lagrangian specific volume of the fluid phase

⁴¹¹ To compute the Lagrangian value of the specific volume of the fluid phase,
⁴¹² we need to compute the Lagrangian temperature rate as below:

$$T_{f,c}^{n+1} = \frac{(me)_{f,c}^L}{m_{f,c}^L c_v} \quad (73)$$

$$\frac{D_f T_{f,c}}{Dt} = \frac{T_{f,c}^{n+1} - T_{f,c}^n}{\Delta t} \quad (74)$$

⁴¹⁴ As such, the Lagrangian specific volume rate is:

$$\Delta(mv)_{f,c} = V f_{f,c}^\phi \nabla \cdot \mathbf{U} + (\phi_{f,c} \alpha_{f,c} \frac{D_f T_{f,c}}{Dt} - f_{f,c}^\phi \sum_{n=1}^N \phi_{nc} \alpha_{nc} \frac{D_n T_{n,c}}{Dt}) \quad (75)$$

⁴¹⁵ where $f_f^\phi = (\phi_f \kappa_f) / (\sum_{n=1}^N \phi_n \kappa_n)$ and $\mathbf{U} = \nabla \cdot (\sum_{s=1}^{N_s} \phi_{sc} \mathbf{U}_{sc} + \sum_{f=1}^{N_f} \phi_{fc} \mathbf{U}_{f,c})$.

⁴¹⁶ Finally, the Lagrangian specific volume is:

$$(mv)_{f,c}^L = V \bar{\rho}_{f,c}^n v_{f,c}^n + \Delta(mv)_{f,c} \quad (76)$$

⁴¹⁷ *Compute advection term and advance in time*

⁴¹⁸ The time advanced mass, linear momentum, energy and specific volume
⁴¹⁹ are:

$$m_{f,c}^{n+1} = m_{f,c}^L - \Delta t \nabla \cdot (\bar{\rho}_{f,c}^L, \mathbf{U}_{f,FC}^L) \quad (77)$$

$$(m\mathbf{U})_{f,c}^{n+1} = (m\mathbf{U})_{f,c}^L - \Delta t \nabla \cdot ((\bar{\rho}\mathbf{U})_{f,c}^L, \mathbf{U}_{f,FC}^L) \quad (78)$$

$$(me)_{f,c}^{n+1} = (me)_{f,c}^L - \Delta t \nabla \cdot ((\bar{\rho}c_v T)_{f,c}^L, \mathbf{U}_{f,FC}^L) \quad (79)$$

$$(mv)_{f,c}^{n+1} = (mv)_{f,c}^L - \Delta t \nabla \cdot ((\bar{\rho}v)_{f,c}^L, \mathbf{U}_{f,FC}^L) \quad (80)$$

⁴²³ Finally, the state variables of the fluid phases of the next time step are:

$$\bar{\rho}_{f,c}^{n+1} = \frac{m_{f,c}^{n+1}}{V} \quad (81)$$

$$\mathbf{U}_{f,c}^{n+1} = \frac{(m\mathbf{U})_{f,c}^{n+1}}{m_{f,c}^{n+1}} \quad (82)$$

$$T_{f,c}^{n+1} = \frac{(me)_{f,c}^{n+1}}{m_{f,c}^{n+1}} \quad (83)$$

$$v_{f,c}^{n+1} = \frac{(mv)_{f,c}^{n+1}}{m_{f,c}^{n+1}} \quad (84)$$

427 *Interpolate from cell to node of the solid phase*

428 First we interpolate the acceleration, velocity and temperature rate to
429 the node as below:

$$430 \quad \mathbf{a}_{si}^n = \sum S_{ci} d\mathbf{U}_{sc}^L \quad (85)$$

$$430 \quad \mathbf{U}_{si}^{n+1} = \sum S_{ci} d\mathbf{U}_{sc}^L \Delta t \quad (86)$$

$$431 \quad dT_{si}^n = \sum S_{ci} dT_{sc}^L \quad (87)$$

432 Then the boundary condition and contact forces f_{si}^{fric} are applied to the nodal
433 velocity, and then accelerations are modified by:

$$434 \quad \mathbf{a}_{si}^n = \frac{\mathbf{v}_{si}^{n+1} - \mathbf{v}_{si}^n}{\Delta t} \quad (88)$$

434 *Update the particle variables*

435 The state variables of the solid phase $[\mathbf{U}_{sp}^{n+1}, \mathbf{x}_{sp}^{n+1}, \nabla \mathbf{U}_{sp}^{n+1}, T_{sp}^{n+1}, \nabla T_{sp}^{n+1}, \mathbf{F}_{sp}^{n+1}, V_{sp}^{n+1}]$
436 (velocity, position, velocity gradient, temperature, temperature gradient, de-
437 formation gradient, volume) are updated as:

$$438 \quad \mathbf{U}_{sp}^{n+1} = \mathbf{U}_{sp}^n + \sum S_{sp} \mathbf{a}_{si}^n \Delta t \quad (89)$$

$$438 \quad \mathbf{x}_{sp}^{n+1} = \mathbf{x}_{sp}^n + \sum S_{sp} \mathbf{U}_{si}^{n+1} \Delta t \quad (90)$$

$$439 \quad \nabla \mathbf{U}_{sp}^{n+1} = \sum \nabla S_{sp} \mathbf{U}_{si}^{n+1} \quad (91)$$

$$440 \quad T_{sp}^{n+1} = T_{sp}^n + \sum S_{sp} dT_{si}^n \Delta t \quad (92)$$

$$441 \quad \nabla T_{sp}^{n+1} = \sum \nabla S_{sp} T_{sp}^n \Delta t \quad (93)$$

$$442 \quad \mathbf{F}_{sp}^{n+1} = (\mathbf{I} + \nabla \mathbf{U}_{sp}^{n+1} \Delta t) \mathbf{F}_{sp}^n \quad (94)$$

$$443 \quad V_{sp}^{n+1} = \det(\mathbf{F}_{sp}^{n+1}) V_{sp}^o \quad (95)$$

444 Finally, the effective stress $(\boldsymbol{\sigma}')^{n+1}$ is updated from the constitutive model
445 and the pore water pressure is interpolated from the cell as:

$$446 \quad p_f^{n+1} = \sum S_{si} P_c^{n+1} \quad (96)$$

446 **Numerical examples**

447 All input files and the analytical calculations in this section are provided
 448 in the Github repository (https://github.com/QuocAnh90/Uintah_NTNU)
 449 for the reproduction of the numerical results.

450 To prevent repetition, we present the parameters of water and air, which
 451 remain consistent across all simulations. The water has a bulk modulus of 2
 452 GPa, a density of 998 kg/m³ at a reference temperature of 5 degrees Celsius
 453 and a reference pressure of 10325 Pa (1atm), a dynamic viscosity μ_f of 1
 454 mPa s). The air has a ideal gas with a density of 1.17 kg/m³ at a reference
 455 temperature of 5 degrees Celsius and a reference pressure of 10325 Pa (1atm),
 456 a dynamic viscosity μ_f of $18.45E^{-3}$ mPa s).

457 *Fluid Flow through isothermal porous media*

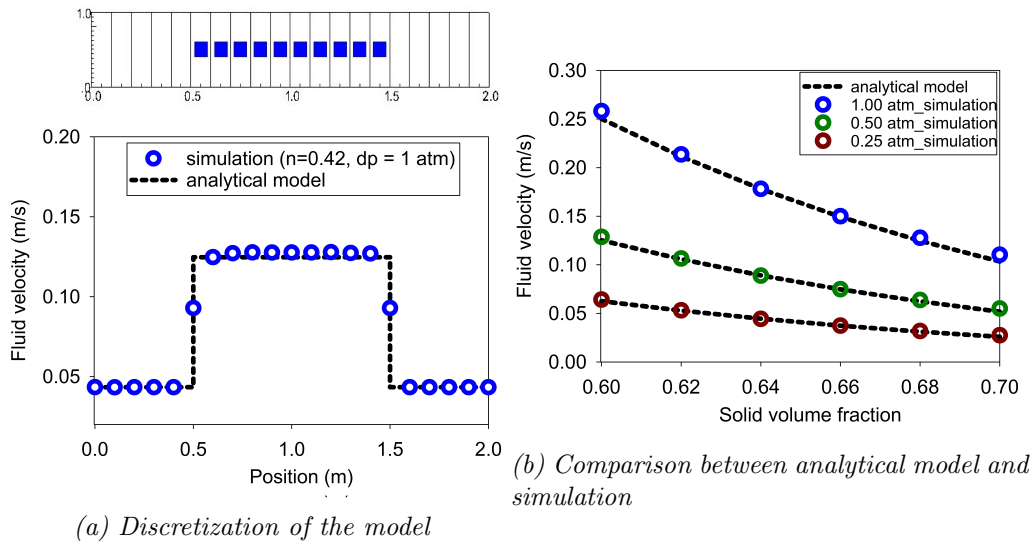


Figure 7: Numerical results of the fluid flow through isothermal porous media

458 Fluid flow through porous media is important in many engineering disci-
 459 plines, like predicting water flow in soil. Fluid flow velocity in one dimension
 460 can be calculated from the porous media's hydraulic conductivity K as:

461

$$U_f = K \frac{\Delta p_f}{L} \quad (97)$$

462 If the Carman-Kozeny formula is adopted $F = 10\phi_s/(1 - \phi_s)^2$, the hydraulic
 463 conductivity will be expressed as $K = D_p^2(1 - \phi_s)^3\rho_f g/180\phi_s^2\mu_f$. Then, the
 464 analytical formula of average velocity in one dimension through the porous
 465 media is:

466

$$U_f = \frac{1}{n} \frac{D_p^2(1 - \phi_s)^3}{180\phi_s^2\mu_f} \frac{\Delta p_f}{L} \quad (98)$$

467 Our numerical model is validated by modeling fluid flow through a 1m
 468 long porous media. The porous media is modeled by elastic material with
 469 Young's modulus is 10 MPa, Poisson's ratio is 0.3, and density is 2650 kg/m³.
 470 The volume fraction of porous media ϕ_s is [0.6, 0.62, 0.66, 0.68, 0.7] and the
 471 average grain diameter d is 1mm. The model is discretized in 20 finite element
 472 and the porous media in 10 finite element with 1 material point per element.
 473 The pressure gradient is applied with three different value [0.25, 0.5, 1] atm.
 474 Figure 7 shows a good agreement of fluid flow prediction between the theory
 475 and the model.

476 *Isothermal consolidation*

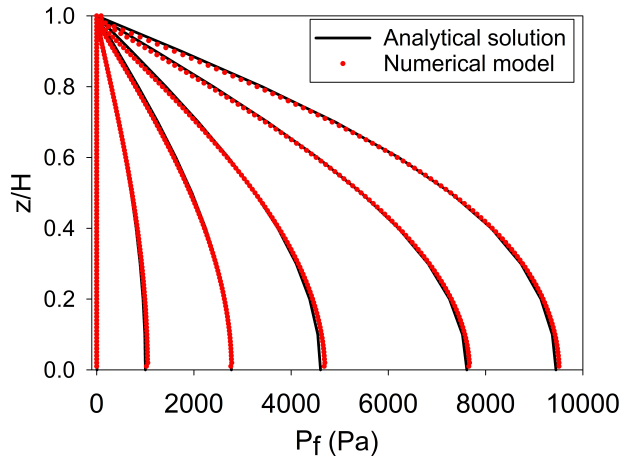


Figure 8: Comparison between analytical solution and numerical solution

477 A common benchmark for a fully saturated porous media is the simulation
 478 of one-dimensional consolidation. Using the Carman-Kozeny formula, the

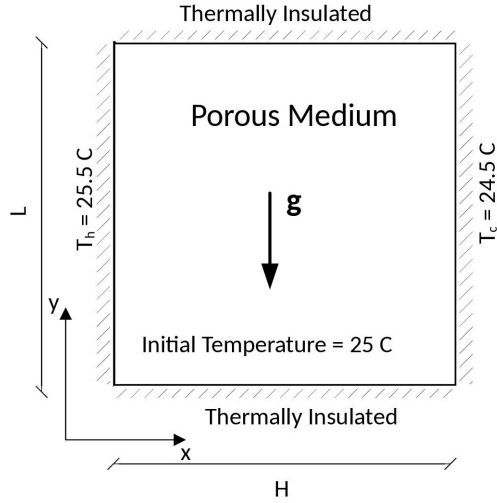


Figure 9: Model schematic [23]

479 time-dependent pressure can be calculated as:

$$p_f = \sum_{m=1}^{\infty} \frac{2F_{ext}}{M} \sin\left(\frac{Mz}{H}\right) e^{-M^2 T_v} \text{ with } M = \frac{\pi}{2}(2m+1) \quad (99)$$

480 where the consolidation rate $T_v = C_v t / H^2$, the consolidation coefficient $C_v =$
 481 $E_v n^3 d^2 / (180(1-n)^2 \mu)$ and the Oedometer modulus $E_v = E(1-v)/(1+v)/(1-2v)$. Our numerical model is validated by modeling the consolidation
 482 of a 1m column. The porous media is modeled by elastic material with
 483 Young's modulus is 10 MPa, Poisson's ratio is 0.3, and density is 2650 kg/m³.
 484 The volume fraction of porous media ϕ_s is 0.7 which is equivalent to the
 485 porosity of 0.3 and the average grain diameter d is 1mm. The model is
 486 discretized in 100 finite element with 1 material point per element. The
 487 external pressure applies to the top of the column is 10 kPa. Figure 8 shows
 488 a good agreement of fluid flow prediction between the theory and the model.
 489

490 *Thermal induced cavity flow*

491 Another benchmark is the thermal induced cavity flow in porous me-
 492 dia. Temperature and velocity distributions are calculated for a square non-
 493 deformable saturated porous media. The top and bottom walls are insulated,
 494 and the left and right walls are at fixed temperature gradient of 1 degree. The
 495 fluid motion at steady state are cavity flow due to the temperature induced

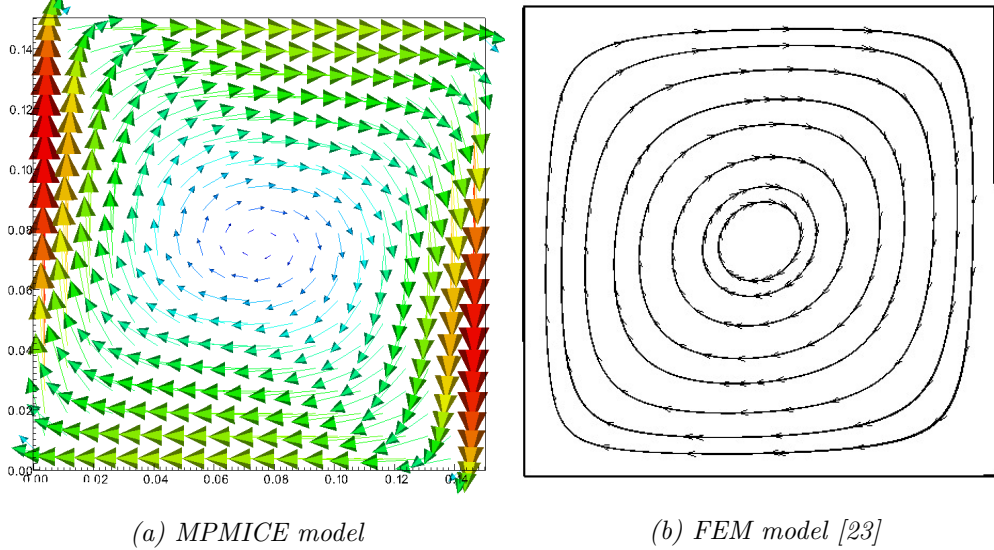


Figure 10: Comparison between MPMICE model and FEM model

496 density variation. The numerical is validated by comparing with the numeri-
 497 cal solution of the finite element method. The porous media is modeled
 498 by non deformable material, and density is 2500 kg/m³. The specific heat
 499 capacity of the water and porous skeleton are 4181 J/kg.K and 835 J/kg.K
 500 respectively. The thermal conductivity of the water and porous skeleton are
 501 0.598 W/m.K and 0.4 W/m.K. The volume fraction of porous media ϕ_s is 0.6
 502 which is equivalent to the porosity of 0.4 and the average grain diameter d is
 503 1mm. The model is discretized in 20 x 20 finite element with 4 material point
 504 per element. Figure 10 shows a good agreement of numerical results of the
 505 model compared with the numerical solution of the finite element method.

506 Underwater debris flow

507 The numerical example is validated using the experimental work of Rzad-
 508 kiewicz et al. on submarine debris flow [24]. In their experiment, sand within
 509 a triangular box is released and slides along a rigid bed inclined at 45 degrees
 510 under water (see Figure 11). The material properties in the numerical model
 511 are selected based on the experiment by Rzadkiewicz et al. [24]. The sand
 512 is characterized by a saturated density of 1985 kg/m³ and a friction angle
 513 of 10 degrees. The effect of Young's modulus on debris flow run-out is neg-
 514 ligible due to the extreme deformation of the debris, so a Young's modulus

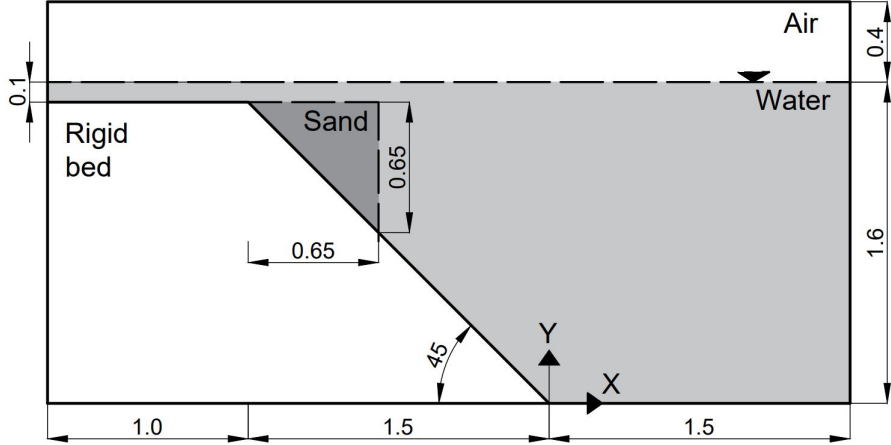


Figure 11: Model schematic

of 50 MPa with a Poisson's ratio of 0.25 is chosen. The rigid bed, being much stiffer, has bulk modulus and shear modulus values of $117E^7$ Pa and $43.8E^7$ Pa, respectively. The numerical parameters used in this example are presented in Table 1.

The boundary conditions imposed in the numerical model are as follows: on all boundary faces, the velocity is set to zero ($U = 0$ m/s) and the temperature is set to 5 degrees Celsius ($T = 5^\circ\text{C}$). At the top boundary, the pressure has a Neumann boundary condition of $d\bar{p}/dx = 0$ kPa, and the density has a Neumann boundary condition of $d\rho/dx = 0 \text{ kg/m}^3$. The background mesh consists of 700×400 cells, resulting in a total of 280,000 cells. Each cell in the debris flow and rigid bed contains 2×2 material points.

Figure 13b illustrates snapshots of the underwater debris flow sliding, demonstrating that the model captures the typical hydroplaning mechanism of the debris flow. Hydroplaning refers to the lifting of the debris flow, causing it to lose contact with the bottom layer. The elevation of the free surface at 0.4s and 0.8s is compared between our proposed method and other methods in Figure 12. Our computed results align well with the experimental results [7].

Unlike other computational models that rely on total stress analysis [5, 6, 7, 8], our proposed model utilizes effective stress analysis, enabling the analysis of water pressure and temperature within the debris flow. Additionally, we investigate the differences between underwater debris flow and saturated debris flow in terms of their interaction with obstacles. Figure 13 presents

538 snapshots of simulations of both underwater and saturated debris flow. The
 539 saturated debris flow (Figure 13a) exhibits behavior similar to frictional flow,
 540 where grains have contact forces with each other. Conversely, the underwa-
 541 ter debris flow (Figure 13b) behaves like turbulent flow, with grains being
 542 separated from each other and exhibiting no contact forces (as reflected by
 the near-zero effective stress in the turbulence domain).

Materials	Bulk modul (Pa)	Shear modul (Pa)	Density (kg/m ³)	Temp (C)	Dynamic viscosity (Pa s)	Friction angle (degrees)
Water (at surface)	2.15e9	-	999.8	5	855e-6	-
Air (at top boundary)	-	-	1.177	5	18.45e-6	-
Sand (porous media)	8.33e6	20e6	1985	5	-	10
Rigid bed (solid)	117e7	43.8e7	8900	5	-	-

Table 1: Numerical parameters for the underwater submarine debris

543

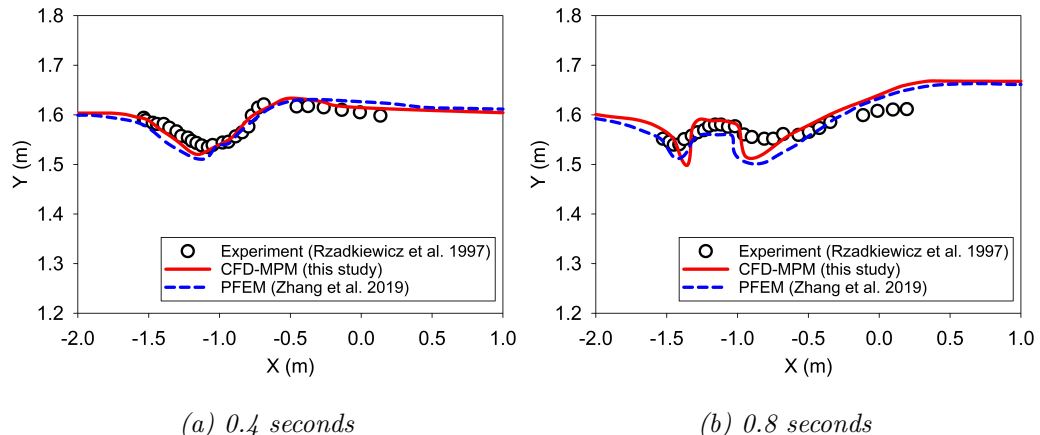


Figure 12: Evolution of water level in the simulation of underwater debris flow

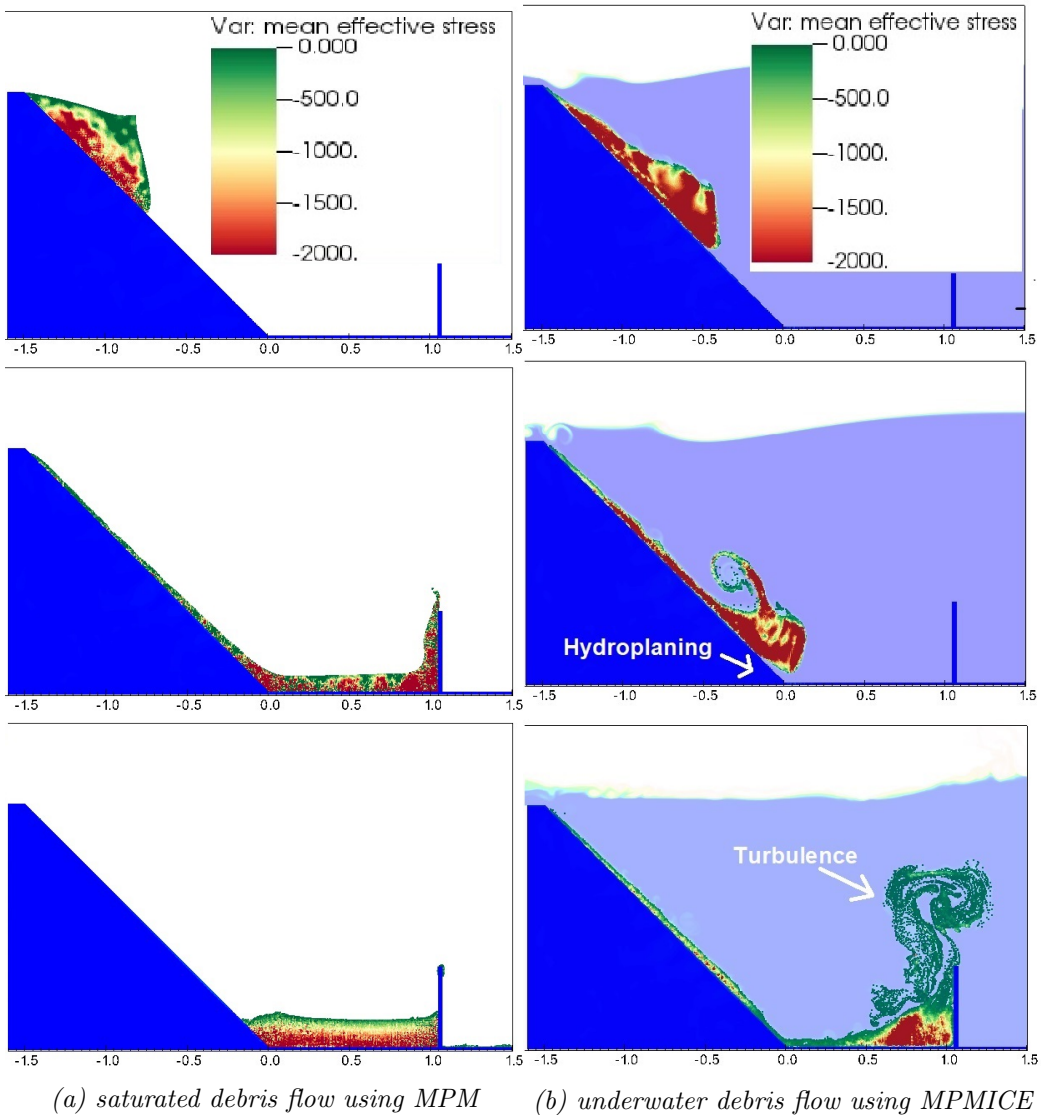


Figure 13: Simulation of Debris Flow: Mean Effective Stress Distribution (Green Color Indicates Near-Zero Effective Stress)

544 Validation of soil response to the seismic loading

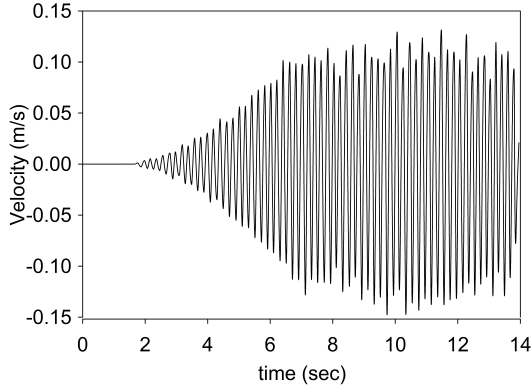


Figure 14: Seismic loading

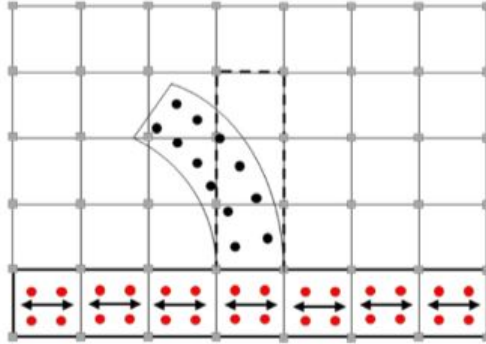


Figure 15: Material points prescribed velocity as kinematic boundary condition [25]

545 An experimental study conducted by Hiraoka et al. [26] aimed to invest-
546 tigate the influence of seismic shaking on the deformation of a 0.5 m-high
547 sand slope. The sand used in the experiment was partially saturated, with a
548 moisture content of 10 percent. The provided soil parameters for the Mohr
549 Coulomb model include the effective friction angle of 23 degrees, apparent
550 cohesion of 0.78 kPa, Young's modulus of 2.57 MPa, and Poisson's ratio of
551 0.33, and moist unit weight of 16.5 kN/m³. The soil's dilatancy angle was
552 assumed to be 0 [26]. The experimental setup consisted of a shaking table
553 box with a steel horizontal base and smooth glass vertical sidewalls. Laser

554 sensors were used to monitor the displacement of the slope's toe and crest.
555 Figure 14 displays the velocity-time history employed in the experiment.

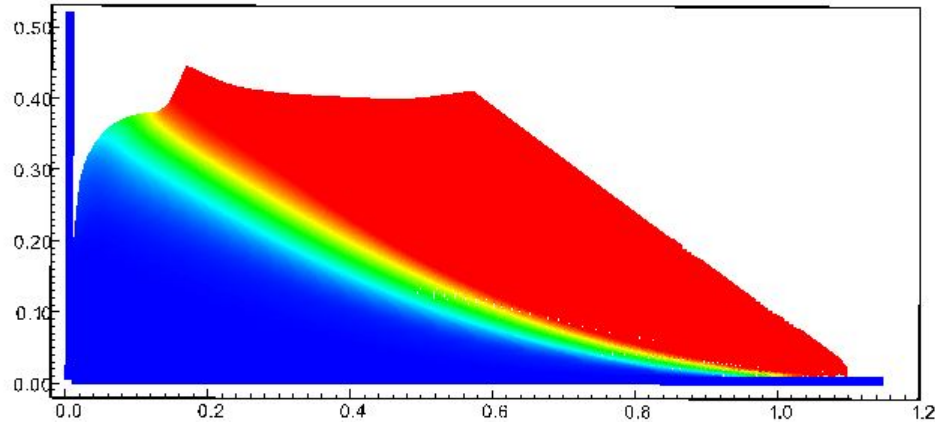


Figure 16: Numerical model of the seismic-induced slope failure with displacement color

556 To simulate the seismic loading in our numerical model, we adopted a
557 method presented by Alsardi et al. [25], which involves specifying the velocity
558 at the corresponding material points representing either the shaking table or
559 the bedrock at the site (see Figure 15). In our simulation, we considered the
560 horizontal base to be fully rough and the vertical contact to be fully smooth.
561 The initial stress condition was initiated using gravity and seismic loading
562 induced the slope failure (see Figure 16).
563 Previous studies by Bhandari et al. [27], Alsardi et al. [25], and Hiraoka et
564 al. [26] attempted to model this experiment using MPM and SPH models. In
565 this study, we compared our results with those obtained from other particle-
566 based methods (Figure 17). The main difference is that we did not apply
567 5 percent numerical damping in our model, unlike the other methods. We
568 found that the final displacement of the slope toe in our MPM model was
569 higher than that observed in the experiment. Nevertheless, the validation of
570 the Mohr-Coulomb model under seismic response demonstrated a reasonable
571 soil behavior in terms of displacement.

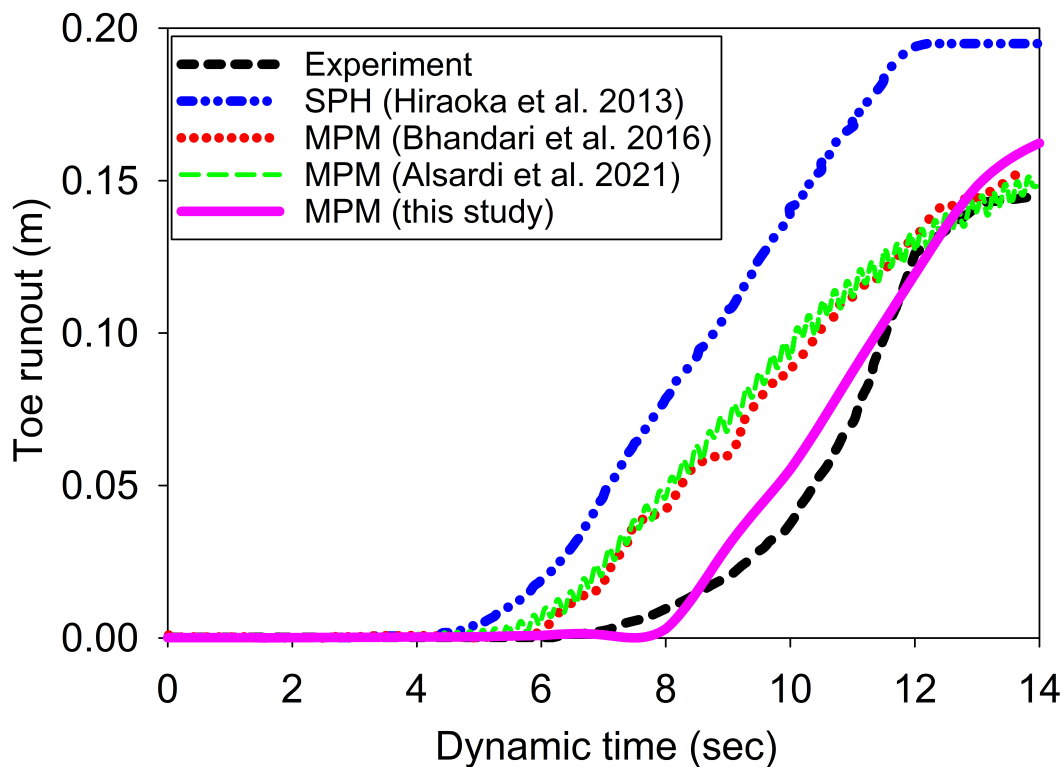


Figure 17: Displacement of the toe of the slope

572 Earthquake-induced submarine landslides

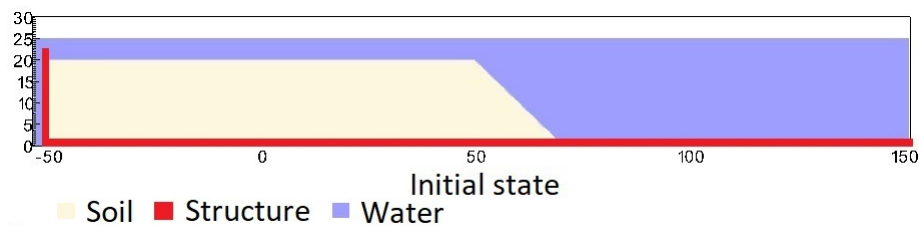


Figure 18: Numerical simulation of the earthquake-induced submarine landslide

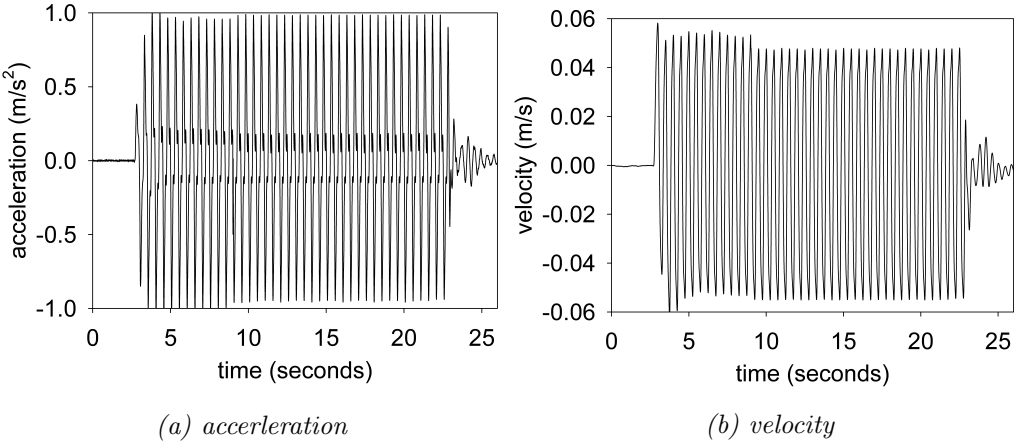


Figure 19: Ground acceleration profile, frequency of 2Hz and magnitude of 1g

573 In the final example, we perform numerical analysis of the earthquake
 574 induced submarine landslides. A plane strain model with the slope under
 575 water is shown in Figure 18. A 20m high slope with slope gradient of 45
 576 degrees is placed in a horizontal and vertical structure which was used to
 577 be a scaling table to apply earthquake loading. We simplify the earthquake
 578 loading by simulating the ground shaking for 20 seconds with the constant
 579 ground acceleration of 1g and a constant frequency of 2Hz (Figure 19a). The
 580 ground motion is applied in terms of velocity (Figure 19b). An earthquake
 581 of this magnitude is possible. For instance, in the case of the 2023 Turkey-
 582 Syria Earthquake, significant ground shaking with peak ground acceleration
 583 exceeding 1g was observed at numerous locations. This serves as an example
 584 of the practical occurrence of such high levels of ground acceleration during
 585 seismic events. To generate the seismic loading, the same method was used
 586 as presented in the previous numerical example.

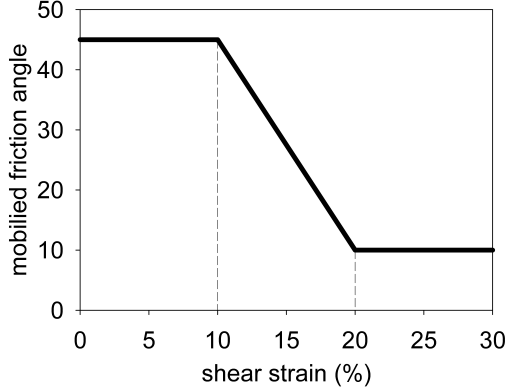


Figure 20: Mobilized friction angle in Mohr Coulomb model

587 A non-associated Mohr-Coulomb model is used for the soil. The soil grain
 588 has the density of 2650 kg/m^3 , Young's modulus of 10 kPa and Poisson's
 589 ratio of 0.3 and zero cohesion. The mobilized friction angle ϕ'_m is governed
 590 following the softening curve (see Figure 20) with the peak friction angle ϕ'_p
 591 of 45 degrees and the residual friction angle ϕ'_r of 10 degrees. The porosity
 592 is 0.3 and the average grain size of the soil is around $0.1 \mu\text{m}$ to mimic the
 593 undrained behavior. The mobilized dilatancy angle is calculated from the
 594 Rowe's stress dilatancy theory [28] as follow:

$$\sin \psi'_m = \frac{\sin \phi'_m - \sin \phi'_r}{1 - (\sin \phi'_r \sin \phi'_m)} \quad (100)$$

595 The solid plane is modeled as a rigid body acted as a shaking table. The
 596 contact between horizontal plane and the sand is the frictional contact with
 597 the friction coefficient of 0.1. No artificial damping is applied in the simu-
 598 lation. The contact between vertical plane and the sand is considered to be
 599 smooth with zero friction coefficient. On all boundary faces, the symmet-
 600 ric boundary condition is imposed, while the Neumann boundary condition
 601 is imposed at the top boundary for pressure ($d\rho/dx = 0 \text{ kPa}$) and density
 602 ($d\rho/dx = 0 \text{ kg/m}^3$). Symmetric boundary condition refers to a condition
 603 where the normal component of the velocity at the boundary face is set to
 604 zero, and the tangential component is equal to the tangential component of
 605 the neighboring cells. The mesh size is $0.25 \times 0.25 \text{ m}$ with 300852 element
 606 cells and 142316 material points. The simulation takes a couple of hours to
 607 perform 60 seconds of the simulation using 4096 CPUs.

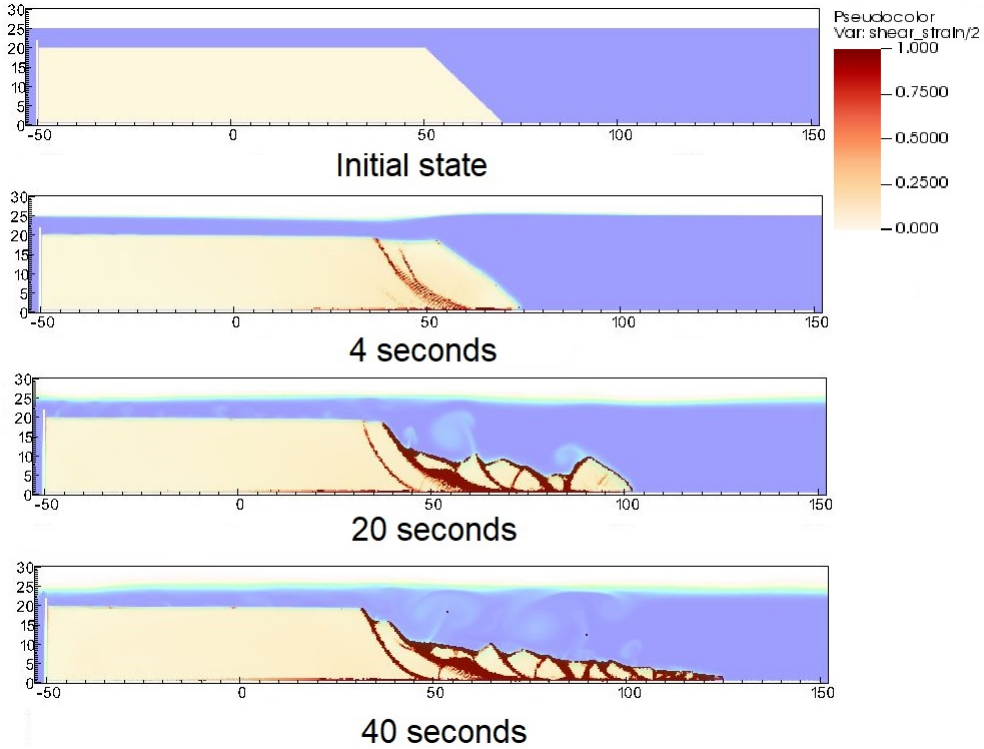


Figure 21: Shear strain during the earthquake-induced submarine landslides

608 We demonstrate the entire process and the mechanism of the earthquake-
 609 induced submarine landslides by showing the shear strain (Figure 21), the
 610 pore water pressure in atm (Figure 22) and the velocity (Figure 23). The
 611 failure mechanism can be characterized as the progressive failure mechanism.
 612 Here are some numerical observation:

- 613 1. At the initial of the seismic event, the seismic loading triggers the
 614 first slide at 3 seconds. At 4 seconds, the debris start to move with the
 615 maximum speed of around 2-3 m/s with multiple shear band developed
 616 in the slope. The wave generated from the submarine slide is around
 617 2-3m towards the slide direction.

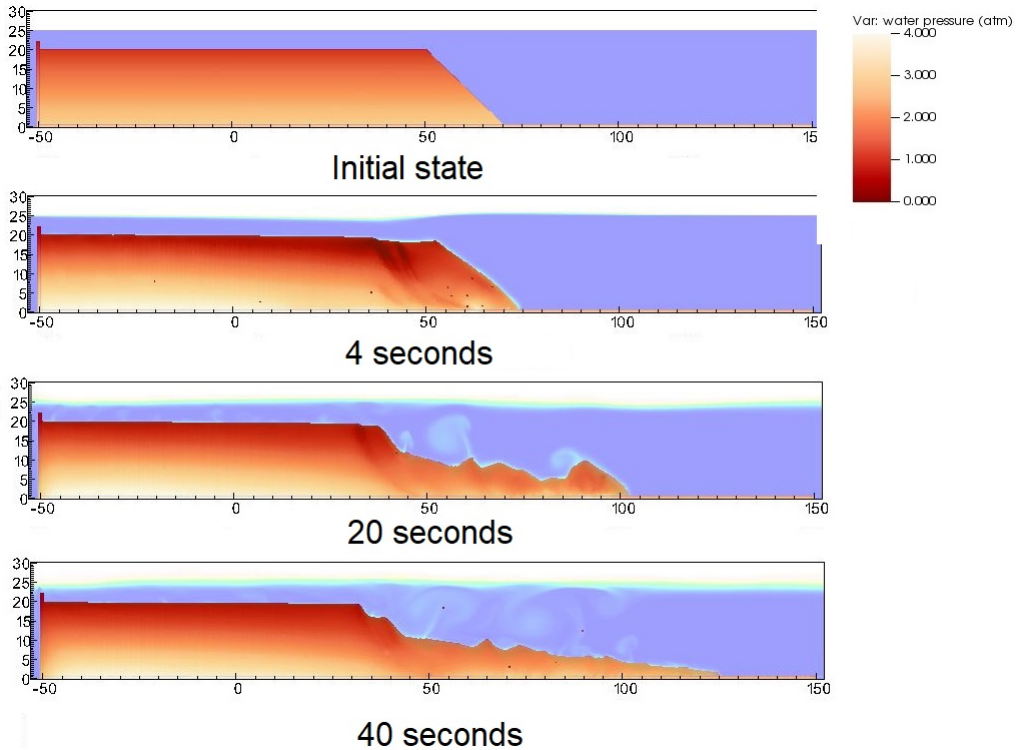


Figure 22: pore water pressure during the earthquake-induced submarine landslides

- 618 2. When the onset of the shear band occurs in the slope (for example
 619 at 4 seconds and 20 seconds), the negative excess pore water pressure
 620 is developed along this shear band with pore water pressure is under
 621 1atm. This is a typical dilatancy behavior when the soil is sheared
 622 rapidly in the undrained behavior.
- 623 3. When the seismic loading ends at 23 seconds, the last shear band is
 624 mobilized and the slope soon reaches to the final deposition. No more
 625 progressive failure developed in the slope. The turbulent flow developed
 626 as the interaction between debris flow and seawater.
- 627 Overall, we show the completed process of the earthquake-induced submarine
 628 landslides involving (1) earthquake triggering mechanism, (2) the onset of the
 629 shear band with the development of negative excess pore water pressure, (3)
 630 progressive failure mechanism, (4) submarine landslide induced wave to final
 631 deposition.

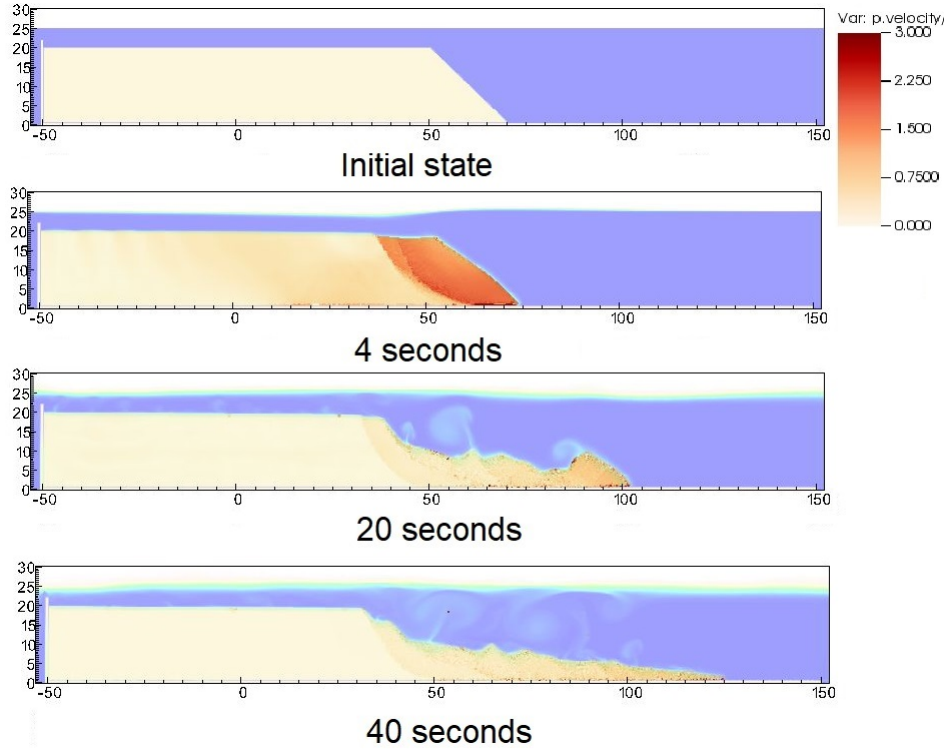


Figure 23: Velocity during the earthquake-induced submarine landslides

632 **Conclusions**

633 We have presented a numerical approach MPMICE for the simulation
 634 of large deformation soil-fluid-structure interaction, emphasizing the simu-
 635 lation of the earthquake-induced submarine landslides. The model uses (1)
 636 the Material Point Method for capturing the large deformation of iso-thermal
 637 porous media and solid structures and (2) Implicit Continuous Eulerian (com-
 638 pressible, conservative multi-material CFD formulation) for modeling the
 639 complex fluid flow including turbulence. This model is implemented in the
 640 high-performance Uintah computational framework and validated against an-
 641 alytical solution and experiment. We then demonstrate the capability of the
 642 model to simulate the entire process of the earthquake induced submarine
 643 landslides.

644 **Acknowledgements**

645 The authors gratefully acknowledge Dr. James Guilkey and Dr. Todd
 646 Harman from the University of Utah for sharing the insight on the theoretical
 647 framework of MPMICE which this work is based. This project has received
 648 funding from the European Union's Horizon 2020 research and innovation
 649 program under the Marie Skłodowska-Curie Actions (MSCA) Individual Fel-
 650 lowship (Project SUBSLIDE "Submarine landslides and their impacts on
 651 offshore infrastructures") grant agreement 101022007. The authors would
 652 also like to acknowledge the support from the Research Council of Norway
 653 through its Centers of Excellence funding scheme, project number 262644
 654 Porelab. The computations were performed on High Performance Comput-
 655 ing resources provided by UNINETT Sigma2 - the National Infrastructure
 656 for High Performance Computing and Data Storage in Norway.

657 **Appendix: Equation derivation**

658 Before deriving the governing equation, we define the Lagrangian deriva-
 659 tive for a state variable f as:

$$\frac{D_f f}{Dt} = \frac{\partial f}{\partial t} + \mathbf{U}_f \cdot \nabla f \quad \frac{D_s f}{Dt} = \frac{\partial f}{\partial t} + \mathbf{U}_s \cdot \nabla f \quad (101)$$

660 we use some definition following [16] as below:

$$-\frac{1}{V} \left[\frac{\partial V_f}{\partial p} \right] \equiv \kappa_f \quad \text{isothermal compressibility of fluid} \quad (102)$$

$$\frac{1}{V} \left[\frac{\partial V_f}{\partial T} \right] \equiv \alpha_f \quad \text{constant pressure thermal expansivity of fluid} \quad (103)$$

661 Then, the rate of volume with incompressible solid grains are calculated as
 662 belows:

$$\frac{1}{V} \frac{D_f V_f}{Dt} = \frac{1}{V} \left(\left[\frac{\partial V_f}{\partial p} \right] \frac{D_f P_{eq}}{Dt} + \left[\frac{\partial V_f}{\partial T_f} \right] \frac{D_f T_f}{Dt} \right) = \frac{1}{V} \left(-\kappa_f \frac{D_f P_{eq}}{Dt} + \alpha_f \frac{D_f T_f}{Dt} \right) \quad (104)$$

663 *Evolution of porosity*

664 Solving the solid mass balance equation (4) with the definition of solid
 665 mass in equation (2), it leads to the rate of porosity as belows:

$$\frac{D_s m_s}{Dt} = \frac{D_s (\phi_s \rho_s V)}{Dt} = \rho_s V \frac{D_s \phi_s}{Dt} + \phi_s V \frac{D_s \rho_s}{Dt} + \phi_s \rho_s \frac{D_s V}{Dt} = 0 \quad (105)$$

₆₆₆ The soil grains are assumed to be incompressible, therefore, term 2 in the
₆₆₇ right hand side is zero. leading to:

$$V \frac{D_s \phi_s}{Dt} + \phi_s \frac{D_s V}{Dt} = 0 \quad (106)$$

₆₆₈ Dividing all terms with V with the equation $\frac{1}{V} \frac{D_s V}{Dt} = \nabla \cdot \mathbf{U}_s$, it leads to:

$$\frac{D_s n}{Dt} = \frac{\partial n}{\partial t} + \mathbf{U}_s \cdot \nabla n = \phi_s \nabla \cdot \mathbf{U}_s \quad (107)$$

₆₆₉ *Momentum conservation*

₆₇₀ The linear momentum balance equations for the fluid phases based on
₆₇₁ mixture theory are:

₆₇₂

$$\frac{1}{V} \frac{D_f(m_f \mathbf{U}_f)}{Dt} = \nabla \cdot (-\phi_f p_f \mathbf{I}) + \nabla \cdot \boldsymbol{\tau}_f + \bar{\rho}_f \mathbf{b} + \sum \mathbf{f}_d + \mathbf{f}_b \quad (108)$$

₆₇₃ On the right hand sand, the first term is the divergence of partial fluid phase
₆₇₄ stress, the third term is the body force, the fourth term is the drag force
₆₇₅ (momentum exchange) and the fifth term is the buoyant force described in
₆₇₆ [29] for the immiscible mixtures. The buoyant force is in the form as belows:

$$\mathbf{f}_b = \boldsymbol{\sigma}_f \nabla(n) \quad (109)$$

₆₇₇ As a result, the linear momentum balance equations for the fluid phases
₆₇₈ become as:

$$\frac{1}{V} \frac{D_f(m_f \mathbf{U}_f)}{Dt} = \frac{1}{V} \left[\frac{\partial(m_f \mathbf{U}_f)}{\partial t} + \nabla \cdot (m_f \mathbf{U}_f \mathbf{U}_f) \right] = -\phi_f \nabla p_f + \nabla \cdot \boldsymbol{\tau}_f + \bar{\rho}_f \mathbf{b} + \sum \mathbf{f}_d \quad (110)$$

₆₇₉ The Reynolds stress component can be included in the term $\boldsymbol{\tau}_f$ to consider the
₆₈₀ turbulent effects if needed. To derive the linear momentum balance equation
₆₈₁ for the solid phase, we begin with the linear momentum balance equation for
₆₈₂ the mixture as:

$$\frac{1}{V} \frac{D_f(m_f \mathbf{U}_f)}{Dt} + \frac{1}{V} \frac{D_s(m_s \mathbf{U}_s)}{Dt} = \nabla \cdot (\boldsymbol{\sigma}) + \bar{\rho}_f \mathbf{b} + \bar{\rho}_s \mathbf{b} \quad (111)$$

₆₈₃ Combining Terzaghi's equation (3) and subtracting both sides with equation
₆₈₄ (110), we obtain the linear momentum balance equations for the solid phase
₆₈₅ as:

$$\frac{1}{V} \frac{D_s(m_s \mathbf{U}_s)}{Dt} = \nabla \cdot (\boldsymbol{\sigma}') - \phi_s \nabla p_f + \bar{\rho}_s \mathbf{b} - \sum \mathbf{f}_d + \sum \mathbf{f}_{fric} \quad (112)$$

₆₈₆ Here the \mathbf{f}_{fric} stems from the soil-structure interaction following the contact
₆₈₇ law between the soil/structure interfaces.

688 *Energy conservation*

689 We adopt the general form of the total energy balance equation for the
 690 porous media from [30], the total energy balance equations for the fluid phases
 691 are:

$$\frac{1}{V} \frac{D_f(m_f(e_f + 0.5\mathbf{U}_f^2))}{Dt} = \nabla \cdot (-np_f \mathbf{I}) \cdot \mathbf{U}_f + \nabla \cdot \mathbf{q}_f + (\bar{\rho}_f \mathbf{b}) \cdot \mathbf{U}_f + \sum \mathbf{f}_d \cdot \mathbf{U}_f + \sum q_{sf} \quad (113)$$

692 Applying the product rule $D(m\mathbf{U}^2) = D(m\mathbf{U} \cdot \mathbf{U}) = 2\mathbf{U} \cdot D(m\mathbf{U})$, the left
 693 hand side of equation (113) becomes:

694

$$\frac{1}{V} \frac{D_f(m_f(e_f + 0.5\mathbf{U}_f^2))}{Dt} = \frac{1}{V} \frac{D_f(m_f e_f)}{Dt} + \frac{1}{V} \frac{D_f(m_f \mathbf{U}_f)}{Dt} \cdot \mathbf{U}_f \quad (114)$$

695 Combining equations (110), (113), (114), we obtain the final form of the
 696 internal energy balance equation for the fluid phases as:

$$\frac{1}{V} \frac{D_f(m_f e_f)}{Dt} = \frac{1}{V} \left[\frac{\partial(m_f e_f)}{\partial t} + \nabla \cdot (m_f e_f \mathbf{U}_f) \right] = \bar{\rho}_f p_f \frac{D_f v_f}{Dt} + \nabla \cdot \mathbf{q}_f + \sum q_{sf} \quad (115)$$

697 On the right hand side, the terms include the average pressure-volume work,
 698 the average viscous dissipation, the thermal transport and the energy ex-
 699 change between solid and fluid respectively. The heat flux is $\mathbf{q}_f = \bar{\rho}_f \beta_f \nabla T_f$
 700 with β_f being the thermal conductivity coefficient. To derive the internal
 701 energy balance equation for the solid phase, we introduce the rate of the
 702 internal energy for the thermoelastic materials as a function of elastic strain
 703 tensor $\boldsymbol{\epsilon}_s^e$ and temperature T_s as belows:

$$\frac{m_s}{V} \frac{D_s(e_s)}{Dt} = \boldsymbol{\sigma}' : \frac{D_s(\boldsymbol{\epsilon}_s^e)}{Dt} + \frac{D_s(e_s)}{D_s(T_s)} \frac{D_s(T_s)}{Dt} = \boldsymbol{\sigma}' : \frac{D_s(\boldsymbol{\epsilon}_s^e)}{Dt} + c_v \frac{D_s(T_s)}{Dt} \quad (116)$$

704 c_v is the specific heat at the constant volume of the solid materials. The total
 705 energy balance equation for the mixture based on [30] can be written as:

706

$$\begin{aligned} \frac{1}{V} \frac{D_f(m_f(e_f + 0.5\mathbf{U}_f^2))}{Dt} + \frac{1}{V} \frac{D_s(m_s(e_s + 0.5\mathbf{U}_s^2))}{Dt} &= \nabla \cdot (-\phi_f p_f \mathbf{I}) \cdot \mathbf{U}_f \\ &+ \nabla \cdot (\boldsymbol{\sigma}' - \phi_s p_f \mathbf{I}) \cdot \mathbf{U}_s + (-\phi_f p_f \mathbf{I}) : \nabla \mathbf{U}_f + \boldsymbol{\sigma}' : \nabla \mathbf{U}_s \\ &+ (\bar{\rho}_f \mathbf{b}) \cdot \mathbf{U}_f + (\bar{\rho}_s \mathbf{b}) \cdot \mathbf{U}_s + \nabla \cdot \mathbf{q}_f + \nabla \cdot \mathbf{q}_s + \sum \mathbf{f}_d \cdot (\mathbf{U}_f - \mathbf{U}_s) \end{aligned} \quad (117)$$

707 Subtracting equation (117), (116) to equations (113) and (112), we obtained
 708 the internal energy balance equation for solid phase as:

$$\boldsymbol{\sigma}' : \frac{D_s(\epsilon_s^e)}{Dt} + \frac{m_s}{V} c_v \frac{D_s(T_s)}{Dt} = \Delta W_s + \Delta W_{friction} + \nabla \cdot \mathbf{q}_s - \sum q_{sf} \quad (118)$$

709 On the right hand side, the terms include the work rate from frictional sliding
 710 between solid materials $\Delta W_{friction}$, thermal transport and energy exchange
 711 between solid and fluid respectively. The heat flux is $\mathbf{q}_s = \bar{\rho}_s \beta_s \nabla T_s$ with β_s
 712 being the thermal conductivity of the solid materials, the mechanical work
 713 rate $\Delta W_s = \boldsymbol{\sigma}' : \frac{D_s(\epsilon_s^e)}{Dt} = \boldsymbol{\sigma}' : (\frac{D_s(\epsilon_s^e)}{Dt} + \frac{D_s(\epsilon_s^p)}{Dt})$ computed from the constitutive
 714 model with ϵ_s^p is the plastic strain tensor, . By subtracting the term $\boldsymbol{\sigma}' : \frac{D_s(\epsilon_s^e)}{Dt}$,
 715 we get the final form of the energy balance equation as:

$$\frac{m_s}{V} c_v \frac{D_s(T_s)}{Dt} = \boldsymbol{\sigma}' : \frac{D_s(\epsilon_s^p)}{Dt} + \Delta W_{friction} + \nabla \cdot \mathbf{q}_s - \sum q_{sf} \quad (119)$$

716 Advanced Fluid Pressure

717 The discretization of the pressure equation begins with the Lagrangian
 718 cell face velocity and the equation for the pressure as:

$$\bar{\rho}_{f,FC} \frac{\mathbf{U}_{f,FC}^{n+1} - \mathbf{U}_{f,FC}^n}{dt} = n \nabla^{FC} P_{f,c}^{n+1} + \bar{\rho}_{f,FC} \mathbf{b} \quad (120)$$

719

$$\kappa \frac{dP}{dt} = \nabla^c \cdot \mathbf{U}_{f,FC}^{n+1} \quad (121)$$

720 The divergence of the equation (120) with $\nabla \cdot \mathbf{b} = 0$ is:

$$\nabla^c \cdot \mathbf{U}_{f,FC}^{n+1} - \nabla^c \cdot \mathbf{U}_{f,FC}^n = \nabla^c \frac{\Delta t}{\rho_{f,FC}^n} \cdot \nabla^{FC} (P_{f,c}^n + \Delta P_{f,c}^n) \quad (122)$$

721 To solve this equation, we define the cell face intermediate velocity $\mathbf{U}_{f,FC}^*$ as:

$$\bar{\rho}_{f,FC} \frac{\mathbf{U}_{f,FC}^* - \mathbf{U}_{f,FC}^n}{\Delta t} = n \nabla^{FC} P_{f,c}^n + \bar{\rho}_{f,FC} \mathbf{b} \quad (123)$$

722 The divergence of the equation (123) is:

$$\nabla^c \cdot \mathbf{U}_{f,FC}^* - \nabla^c \cdot \mathbf{U}_{f,FC}^n = \nabla^c \frac{\Delta t}{\rho_{f,FC}^n} \cdot \nabla^{FC} P_{f,c}^n \quad (124)$$

723 Combining equations (121, 122, 124), it leads to:

$$\left(\kappa - \nabla^c \frac{\Delta t}{\rho_{f,FC}^n} \cdot \nabla^{FC} \right) \Delta P_{fc}^n = -\nabla^c \cdot \mathbf{U}_{f,FC}^* \quad (125)$$

724 When the fluid is incompressible, κ approaches to zero and the equation
725 (125) becomes the Poisson's equation for the incompressible fluid flow.

726 *Momentum and Energy exchange with an implicit solver*

727 Considering the fluid momentum balance equation as:

$$(m\mathbf{U})_{f,FC}^{n+1} = (m\mathbf{U})_{f,FC}^n - \Delta t(Vn\nabla^{FC}P_{f,c}^n + m_f\mathbf{b}) + VK\Delta t(\mathbf{U}_{s,FC}^{n+1} - \mathbf{U}_{f,FC}^{n+1}) \quad (126)$$

728 And assuming $m_{f,FC}^{n+1} = m_{f,FC}^n$, we get:

$$\mathbf{U}_{f,FC}^{n+1} = \mathbf{U}_{f,FC}^n - \Delta t\left(\frac{\nabla^{FC}P_{fc}^n}{\rho_{f,FC}^n} + \mathbf{b}\right) + \frac{\Delta tK}{\bar{\rho}_{f,FC}^n}(\mathbf{U}_{s,FC}^{n+1} - \mathbf{U}_{f,FC}^{n+1}) \quad (127)$$

729 As defined in the section 'Advanced Fluid Pressure', the cell face intermediate
730 fluid velocity $\mathbf{U}_{f,FC}^* = \Delta t(\nabla^{FC}P_{fc}^n/\rho_{f,FC}^n + \mathbf{b})$ is computed as:

$$\mathbf{U}_{f,FC}^{n+1} = \mathbf{U}_{f,FC}^* + \frac{\Delta tK}{\bar{\rho}_{f,FC}^n}(\mathbf{U}_{s,FC}^{n+1} - \mathbf{U}_{f,FC}^{n+1}) \quad (128)$$

731 Considering the solid momentum balance equation as:

$$(m\mathbf{U})_{s,FC}^{n+1} = (m\mathbf{U})_{s,FC}^n - \Delta t(V\nabla^{FC} \cdot \boldsymbol{\sigma}'^n - V(1-n)\nabla^{FC}P_{f,c}^n + m_s\mathbf{b}) - VK\Delta t(\mathbf{U}_{s,FC}^{n+1} - \mathbf{U}_{f,FC}^{n+1}) \quad (129)$$

732 We define the cell face intermediate solid velocity as $\mathbf{U}_{s,FC}^* = \Delta t(\nabla^{FC} \cdot \boldsymbol{\sigma}'^n / \bar{\rho}_{s,FC}^n - \nabla^{FC}P_{f,c}^n/\rho_s + \mathbf{b})$ leading to:

$$\mathbf{U}_{s,FC}^{n+1} = \mathbf{U}_{s,FC}^* - \frac{\Delta tK}{\bar{\rho}_{s,FC}^n}(\mathbf{U}_{s,FC}^{n+1} - \mathbf{U}_{f,FC}^{n+1}) \quad (130)$$

734 Combining equation (128) and (130) we get:

$$\begin{aligned} \mathbf{U}_{f,FC}^* + \Delta\mathbf{U}_{f,FC} &= \mathbf{U}_{f,FC}^* + \frac{\Delta tK}{\bar{\rho}_{f,FC}^n}(\mathbf{U}_{s,FC}^* + \Delta\mathbf{U}_{s,FC} - \mathbf{U}_{f,FC}^* - \Delta\mathbf{U}_{f,FC}) \\ \mathbf{U}_{s,FC}^* + \Delta\mathbf{U}_{s,FC} &= \mathbf{U}_{s,FC}^* - \frac{\Delta tK}{\bar{\rho}_{s,FC}^n}(\mathbf{U}_{s,FC}^* + \Delta\mathbf{U}_{s,FC} - \mathbf{U}_{f,FC}^* - \Delta\mathbf{U}_{f,FC}) \end{aligned} \quad (131)$$

735 Rearranging the equation (131), it leads to the linear system of equations as
 736 belows:

$$\begin{vmatrix} (1 + \beta_{12,FC}) & -\beta_{12,FC} \\ -\beta_{21,FC} & (1 + \beta_{21,FC}) \end{vmatrix} \begin{vmatrix} \Delta \mathbf{U}_{f,FC} \\ \Delta \mathbf{U}_{s,FC} \end{vmatrix} = \begin{vmatrix} \beta_{12,FC}(\mathbf{U}_{s,FC}^* - \mathbf{U}_{f,FC}^*) \\ \beta_{21,FC}(\mathbf{U}_{f,FC}^* - \mathbf{U}_{s,FC}^*) \end{vmatrix}$$

737 Solving this linear equations with $\beta_{12,FC} = (\Delta t K) / \bar{\rho}_{f,FC}^n$ and $\beta_{21,FC} =$
 738 $(\Delta t K) / \bar{\rho}_{s,FC}^n$ with K is the momentum exchange coefficient. Similar deriva-
 739 tion can be performed to computed the cell-center velocity increment leading
 740 to:

$$\begin{vmatrix} (1 + \beta_{12c}) & -\beta_{12c} \\ -\beta_{21c} & (1 + \beta_{21c}) \end{vmatrix} \begin{vmatrix} \Delta \mathbf{U}_{f,c} \\ \Delta \mathbf{U}_{sc} \end{vmatrix} = \begin{vmatrix} \beta_{12c}(\mathbf{U}_{sc}^* - \mathbf{U}_{f,c}^*) \\ \beta_{21c}(\mathbf{U}_{f,c}^* - \mathbf{U}_{sc}^*) \end{vmatrix}$$

741 with $\beta_{12c} = (\Delta t K) / \bar{\rho}_{f,c}^n$ and $\beta_{21c} = (\Delta t K) / \bar{\rho}_{sc}^n$ and the cell-centered interme-
 742 diate velocity can be calculated by:

$$\begin{aligned} \mathbf{U}_{f,c}^* &= \mathbf{U}_{f,c}^n + \Delta t \left(-\frac{\nabla P_{f,c}^{n+1}}{\rho_{f,c}^n} + \frac{\nabla \cdot \boldsymbol{\tau}_{f,c}^n}{\bar{\rho}_{f,c}^n} + \mathbf{b} \right) \\ \mathbf{U}_{sc}^* &= \mathbf{U}_{sc}^n + \Delta t \left(\frac{\nabla \cdot \boldsymbol{\sigma}_c'^n}{\bar{\rho}_{sc}^n} - \frac{\nabla P_{f,c}^{n+1}}{\rho_s} + \mathbf{b} \right) \end{aligned} \quad (132)$$

743 For generalize multi materials i,j = 1:N, the linear equations is in the form
 744 as:

$$\begin{vmatrix} (1 + \beta_{ij}) & -\beta_{ij} \\ -\beta_{ji} & (1 + \beta_{ji}) \end{vmatrix} \begin{vmatrix} \Delta \mathbf{U}_i \\ \Delta \mathbf{U}_j \end{vmatrix} = \begin{vmatrix} \beta_{ij}(\mathbf{U}_i^* - \mathbf{U}_j^*) \\ \beta_{ji}(\mathbf{U}_j^* - \mathbf{U}_i^*) \end{vmatrix}$$

745 Similar approach applied for the ernergy exchange term leading to:

$$\begin{vmatrix} (1 + \eta_{ij}) & -\eta_{ij} \\ -\eta_{ji} & (1 + \eta_{ji}) \end{vmatrix} \begin{vmatrix} \Delta T_i \\ \Delta T_j \end{vmatrix} = \begin{vmatrix} \eta_{ij}(T_i^n - T_j^n) \\ \eta_{ji}(T_j^n - T_i^n) \end{vmatrix}$$

746 with η is the energy exchange coefficient.

747 References

- 748 [1] D. Yuk, S. Yim, P.-F. Liu, Numerical modeling of submarine mass-
 749 movement generated waves using RANS model, Computers and Geo-
 750 sciences 32 (7) (2006) 927–935. doi:10.1016/j.cageo.2005.10.028.
 751 URL <https://doi.org/10.1016/j.cageo.2005.10.028>

- 752 [2] S. Glimsdal, J.-S. L'Heureux, C. B. Harbitz, F. Løvholt, The 29th january 2014 submarine landslide at statland, norway—landslide dynamics,
753 tsunami generation, and run-up, *Landslides* 13 (6) (2016) 1435–1444.
754 doi:10.1007/s10346-016-0758-7.
755 URL <https://doi.org/10.1007/s10346-016-0758-7>
- 756 [3] S. Abadie, D. Morichon, S. Grilli, S. Glockner, Numerical simulation of waves generated by landslides using a multiple-fluid navier–stokes model, *Coastal Engineering* 57 (9) (2010) 779–794.
757 doi:10.1016/j.coastaleng.2010.03.003.
758 URL <https://doi.org/10.1016/j.coastaleng.2010.03.003>
- 762 [4] M. Rauter, S. Viroulet, S. S. Gylfadóttir, W. Fellin, F. Løvholt, Granular porous landslide tsunami modelling – the 2014 lake askja flank collapse, *Nature Communications* 13 (1) (Feb. 2022). doi:10.1038/s41467-022-28296-7.
763 URL <https://doi.org/10.1038/s41467-022-28296-7>
- 765 [5] Q.-A. Tran, W. Sołowski, Generalized interpolation material point method modelling of large deformation problems including strain-rate effects – application to penetration and progressive failure problems, *Computers and Geotechnics* 106 (2019) 249–265.
766 doi:10.1016/j.compgeo.2018.10.020.
767 URL <https://doi.org/10.1016/j.compgeo.2018.10.020>
- 773 [6] T. Capone, A. Panizzo, J. J. Monaghan, SPH modelling of water waves generated by submarine landslides, *Journal of Hydraulic Research* 48 (sup1) (2010) 80–84. doi:10.1080/00221686.2010.9641248.
774 URL <https://doi.org/10.1080/00221686.2010.9641248>
- 778 [7] X. Zhang, E. Oñate, S. A. G. Torres, J. Bleyer, K. Krabbenhoft, A unified lagrangian formulation for solid and fluid dynamics and its possibility for modelling submarine landslides and their consequences, *Computer Methods in Applied Mechanics and Engineering* 343 (2019) 314–338. doi:10.1016/j.cma.2018.07.043.
779 URL <https://doi.org/10.1016/j.cma.2018.07.043>
- 783 [8] R. Dey, B. C. Hawlader, R. Phillips, K. Soga, Numerical modelling
784 of submarine landslides with sensitive clay layers, *Géotechnique* 66 (6)

- 785 (2016) 454–468. doi:10.1680/jgeot.15.p.111.
786 URL <https://doi.org/10.1680/jgeot.15.p.111>
- 787 [9] S. Bandara, K. Soga, Coupling of soil deformation and pore fluid flow
788 using material point method, Computers and Geotechnics 63 (2015)
789 199–214. doi:10.1016/j.compgeo.2014.09.009.
790 URL <https://doi.org/10.1016/j.compgeo.2014.09.009>
- 791 [10] A. P. Tampubolon, T. Gast, G. Klár, C. Fu, J. Teran, C. Jiang,
792 K. Museth, Multi-species simulation of porous sand and water
793 mixtures, ACM Transactions on Graphics 36 (4) (2017) 1–11.
794 doi:10.1145/3072959.3073651.
795 URL <https://doi.org/10.1145/3072959.3073651>
- 796 [11] A. S. Baumgarten, K. Kamrin, A general constitutive model for dense,
797 fine-particle suspensions validated in many geometries, Proceedings
798 of the National Academy of Sciences 116 (42) (2019) 20828–20836.
799 doi:10.1073/pnas.1908065116.
800 URL <https://doi.org/10.1073/pnas.1908065116>
- 801 [12] Q.-A. Tran, W. Sołowski, Temporal and null-space filter for the
802 material point method, International Journal for Numerical Methods in
803 Engineering 120 (3) (2019) 328–360. doi:10.1002/nme.6138.
804 URL <https://doi.org/10.1002/nme.6138>
- 805 [13] X. Zheng, F. Pisanò, P. J. Vardon, M. A. Hicks, An explicit stabilised
806 material point method for coupled hydromechanical problems in two-
807 phase porous media, Computers and Geotechnics 135 (2021) 104112.
808 doi:10.1016/j.compgeo.2021.104112.
809 URL <https://doi.org/10.1016/j.compgeo.2021.104112>
- 810 [14] Q. A. Tran, W. Sołowski, M. Berzins, J. Guilkey, A convected particle
811 least square interpolation material point method, International Journal
812 for Numerical Methods in Engineering 121 (6) (2019) 1068–1100.
813 doi:10.1002/nme.6257.
814 URL <https://doi.org/10.1002/nme.6257>
- 815 [15] J.-S. Chen, M. Hillman, S.-W. Chi, Meshfree methods: Progress made
816 after 20 years, Journal of Engineering Mechanics 143 (4) (Apr. 2017).

- 817 doi:10.1061/(asce)em.1943-7889.0001176.
818 URL [https://doi.org/10.1061/\(asce\)em.1943-7889.0001176](https://doi.org/10.1061/(asce)em.1943-7889.0001176)
- 819 [16] B. A. Kashiwa, A multifield model and method for fluid-structure in-
820 teraction dynamics, Tech. Rep. LA-UR-01-1136, Los Alamos National
821 Laboratory (2001).
- 822 [17] J. Guilkey, T. Harman, B. Banerjee, An eulerian-lagrangian
823 approach for simulating explosions of energetic devices,
824 Computers and Structures 85 (11) (2007) 660 – 674.
825 doi:<https://doi.org/10.1016/j.compstruc.2007.01.031>.
826 URL <http://www.sciencedirect.com/science/article/pii/S0045794907000429>
- 827 [18] A. S. Baumgarten, B. L. Couchman, K. Kamrin, A coupled finite volume
828 and material point method for two-phase simulation of liquid-sediment
829 and gas-sediment flows, Computer Methods in Applied Mechanics and
830 Engineering 384 (2021) 113940. doi:10.1016/j.cma.2021.113940.
831 URL <https://doi.org/10.1016/j.cma.2021.113940>
- 832 [19] S. Bardenhagen, J. Guilkey, K. Roessig, J. Brackbill, W. Witzel,
833 J.C.Foster, An improved contact algorithm for the material point
834 method and application to stress propagation in granular material,
835 CMES-Computer Modeling in Engineering and Sciences 2 (2001) 509–
836 522. doi:10.3970/cmes.2001.002.509.
- 837 [20] J. A. M. K. R. Beetstra, M. A. van der Hoef, Drag force of intermediate
838 reynolds number flow past mono- and bidisperse arrays of spheres,
839 Fluid Mechanics and Transport Phenomena 53 (2) (2007) 489 – 501.
840 doi:<https://doi.org/10.1002/aic.11065>.
- 841 [21] R. W. Stewart, The air-sea momentum exchange, Boundary-Layer Me-
842 teorology 6 (1-2) (1974) 151–167. doi:10.1007/bf00232481.
843 URL <https://doi.org/10.1007/bf00232481>
- 844 [22] S. G. Bardenhagen, E. M. Kober, The generalized interpolation material
845 point method, Computer Modeling in Engineering and Sciences 5 (2004)
846 477–496. doi:10.1016/j.compgeo.2021.104199.
847 URL <https://doi.org/10.3970/cmes.2004.005.477>
- 848 [23] S. G. Amiri, E. Taheri, A. Lavasan, A hybrid finite element model for
849 non-isothermal two-phase flow in deformable porous media, Computers

- 850 and Geotechnics 135 (2021) 104199. doi:10.1016/j.compgeo.2021.104199.
851 URL <https://doi.org/10.1016/j.compgeo.2021.104199>
- 852 [24] S. A. R. C. Mariotti;, P. Heinrich, Numerical simulation of sub-
853 marine landslides and their hydraulic effects, Journal of Waterway, Port,
854 Coastal, and Ocean Engineering 123 (4) (1997).
855 doi:[https://doi.org/10.1061/\(ASCE\)0733-950X\(1997\)123:4\(149\)](https://doi.org/10.1061/(ASCE)0733-950X(1997)123:4(149)).
- 856 [25] A. Alsardi, A. Yerro, Runout Modeling of Earthquake-Triggered
857 Landslides with the Material Point Method, pp. 21–31.
858 arXiv:<https://ascelibrary.org/doi/pdf/10.1061/9780784483428.003>,
859 doi:10.1061/9780784483428.003.
860 URL <https://ascelibrary.org/doi/abs/10.1061/9780784483428.003>
- 861 [26] H. N., O. A., B. H. H., R. P., R. Fukagawa, Seismic slope failuremod-
862 ellng using the mesh-free sph method, International Journal of Geomate
863 (2013) 660–665.
- 864 [27] T. Bhandari, F. Hamad, C. Moormann, K. Sharma,
865 B. Westrich, Numerical modelling of seismic slope failure us-
866 ing mpm, Computers and Geotechnics 75 (2016) 126–134.
867 doi:<https://doi.org/10.1016/j.compgeo.2016.01.017>.
868 URL <https://www.sciencedirect.com/science/article/pii/S0266352X16000264>
- 869 [28] D. Muir Wood, Soil behaviour and critical state soil mechanics, Cam-
870 bridge University Press, United Kingdom, 1990.
- 871 [29] D. Drumheller, On theories for reacting immiscible mixtures, Interna-
872 tional Journal of Engineering Science 38 (3) (2000) 347 – 382.
873 doi:[https://doi.org/10.1016/S0020-7225\(99\)00047-6](https://doi.org/10.1016/S0020-7225(99)00047-6).
874 URL <http://www.sciencedirect.com/science/article/pii/S0020722599000476>
- 875 [30] S. Hassanzadeh, Derivation of basic equations of mass transport in
876 porous media, part1: Macroscopic balance laws, Advances in Wa-
877 ter Resources 9 (1986) 196–206. doi:[https://doi.org/10.1016/0309-1708\(86\)90024-2](https://doi.org/10.1016/0309-1708(86)90024-2).